Growth and Study of Si/SiGe Multiple Quantum Wells
for Mid-infrared Applications

Weiwei Zheng

A DISSERTATION
PRESENTED TO THE FACULTY
OF PRINCETON UNIVERSITY
IN CANDIDACY FOR THE DEGREE
OF MASTER OF SCIENCE

RECOMMENDED FOR ACCEPTANCE
BY THE DEPARTMENT OF
ELECTRICAL ENGINEERING

DECEMBER 2007

ABSTRACT

A process for the growth of uniform boron-doped Si/SiGe multiple quantum wells by rapid thermal chemical vapor deposition (RTCVD) for studying intersubband transitions for quantum cascade laser applications has been developed. The doping density profiles are extremely sharp (~2 nm/decade and ~3 nm/decade for the leading and trailing boron edges, respectively) measured by high resolution secondary ion mass spectroscopy (SIMS) and the well to well uniformity is excellent.

The development and exploration of infrared studies on Si/SiGe multiple quantum wells are summarized. The possible obstacles underlying the structure which prohibits the detection of infrared signals are discussed.

The study on the effect of germanium content on the valence band offset of compressively strained $Si_{1-x}Ge_x$/Si(100) heterojunctions by RTCVD has been presented and the mismatch between the experimental and the theoretical band offset values remains unknown.

ACKNOWLEDGEMENTS

I am indebted to many people who have enabled this research and helped me during my time at Princeton.

First, I would like to thank professor Jim Sturm for his constant encouragement and enthusiasm to this project. His insightful hints, intellectual questions and unique way to convey complex concepts in a fundamental way accompanied my intellectual growth. Most importantly, the energy and excitement with which he approaches research and teaching will serve as profound inspiration in my future endeavors. I also thank professor Claire Gmachl for her guidance and support to this project. Her boundless energy and indefatigable enthusiasm for research never cease to amaze me. Without her encouragement and advice, my efforts would have surely been in vain.

Special thanks go to Dr. Nao Yao for spending time with me on TEM measurements. I have lost track of the number of times I have gone to him for advice and help. His unfailing willingness to help is memorable.

I particularly own thanks to past and present fellows of RTCVD crowd, Rebecca Lorenz Peterson, Kun Yao, Keith Chung, Sushobhan Avasthi and Jeremy Booher, for their camaraderie in RTCVD maintenance and service. I am grateful to the rest of the fellow students in Sturm Group for providing such a friendly research environment. I would also like to thank all the members in Gmachl group, particularly, Zhijun Liu and Dan Wasserman, for the countless discussions on a wide range of topics and timely help in the exploration of infrared studies.

Finally, I am forever obliged and offer heartfelt gratitude to my family for the numerous sacrifices they have made. In particular, no words can express my deepest

appreciation and thankfulness to my husband, Feng, who has walked alongside me through the good days and bad.

LIST OF FIGURES

LIST OF TABLES

CONTENTS

CHAPTER 1

INTRODUCTION

1.1 Motivation

The last decade has witnessed a tremendous progress in the field of quantum cascade lasers, which are semiconductor injection lasers based on intersubband transitions in a multiple-quantum-well (MQW) heterostructure, designed by means of band-structure engineering.

The intersubband nature of the optical transition has several key advantages. First, the emission wavelength is primary a function of the QW thickness, which allows choosing well-understood and reliable semiconductors for the generation of light in a wavelength range unrelated to the materials energy band gap. Second, through a cascade process, one electron generating several tens of photons becomes feasible, as the electron remains inside the conduction band throughout its traversal of the active region. Finally, the intersubband transitions are characterized through ultrafast carrier dynamics which has been expected to have significant impact on laser performance.

A typical quantum cascade laser is realized using heteroepitaxy of III-V material systems such as InGaAs/InP. A long-standing wish for microelectronics technology has been the integration of semiconductor lasers onto a silicon chip. Silicon-germanium alloys have brought many of the advantages of heterstructures into the domain of the dominating Si technology, but the indirect band gap of group IV is

a hindrance to Si-based active optical components, which implies that radiative transition across the band gap must be accompanies by a large momentum transfer, and therefore unlikely. The quantum cascade approach constitutes a possible way to integrate active optical components into Si-based technology since the transitions occur within a single band, so called intersubband transitions. Carriers stream down a potential staircase of coupled quantum wells, passing a sequence of active layers, where the lifetimes of two levels are carefully tuned through control of the tunneling probability and phonon interaction strength in order to obtain population inversion. This concept necessitates a transition with a narrow linewidth and an upper state with a sufficient long lifetime.

1.2 Thesis Outline

Chapter 2 reviews the development and exploration of Si-based light emitters and lasers. The strength and weakness of Si-based material systems compared to the conventional III-V material systems have been summarized. The practical considerations in the realization of Si-based QCL by RTCVD deposition are also discussed

Chapter 3 presents the growth and characterization of ultra uniform boron-doped Si/SiGe multiple quantum wells by RTCVD. High resolution SIMS has been performed to study the quantum well uniformity and the sharpness of the doping density. High resolution XTEM has been further confirmed the ultra uniformity of Si/SiGe multiple quantum wells.

Chapter 4 demonstrates the infrared study of the Si/SiGe multiple quantum wells.

Two approaches, multi-pass transmission and photocurrent measurements have been applied. The possible obstacle underlying the structure which might prohibit the infrared detection has been discussed.

Chapter 5 states the study on the effect of Ge content on the band alignment of the strained $Si_{1-x}Ge_x/Si(100)$. The current-voltage method has been used and the results have been interpreted.

Chapter 6 summarizes the contribution of this thesis and suggests the directions along which future work may be pursued.

CHAPTER 2

LONG TERM GOAL: DEVELOPMENT OF SI-BASED LIGHT

EMITTERS AND LASERS

2.1 Introduction

Quantum cascade lasers, which are based on intersubband transitions between quantized states in multiple-QW heterostructures, have attracted an increasing amount of attention since the first experimental demonstration in 1994 [1]. Despite the known ultra-fast carrier relaxation mechanism within one band of a semiconductor, population inversion — which ultimately allows laser action — can be achieved between such states by means of "band-structure-engineering". That entails that QW, barrier thickness and band offsets are designed, engineered, to tailor the fundamental properties of energy levels, carrier scattering rates, optical dipole matrix elements and tunneling time within given fundamental limits, to optimize population densities and transition probabilities for the various energy states.

Fig. 2.1 shows a schematic of a typical quantum cascade laser. The active region basically consists hundreds of stacks of multiple quantum wells, which are typically grown by molecular beam epitaxial (MBE). Fig. 2.2 shows a schematic of the energy diagram and the charge carrier and photon flows in these structures.

Briefly, charge carriers are injected through resonant tunneling into an upper, excited energy level in each active region. From there the charge carriers make optical transition to a lower energy level. Alternatively, nonradiative transitions between

4

excited and lower energy levels are also possible. The charge carriers are extracted from the lower energy level, and from the active region, by scattering into even lower energy levels, and through resonant tunneling. In the following so called injector the charge carriers gain again energy from the applied electrical field and are then injected into the upper energy levels of the following active region.

Laser beam
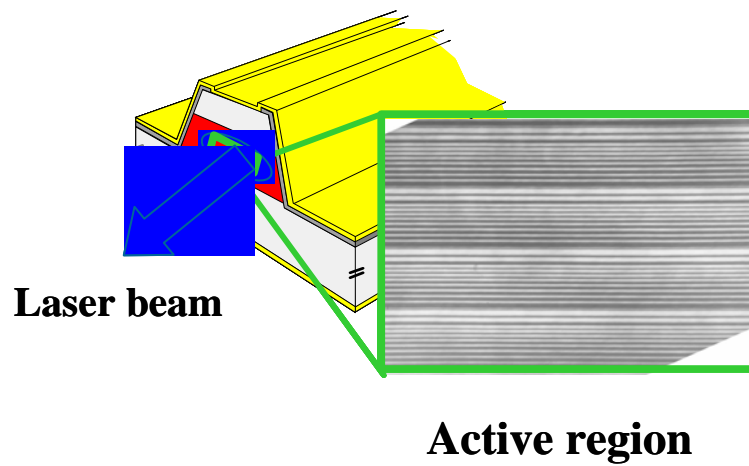
Active region

Fig. 2.1 Schematic of a typical QCL.
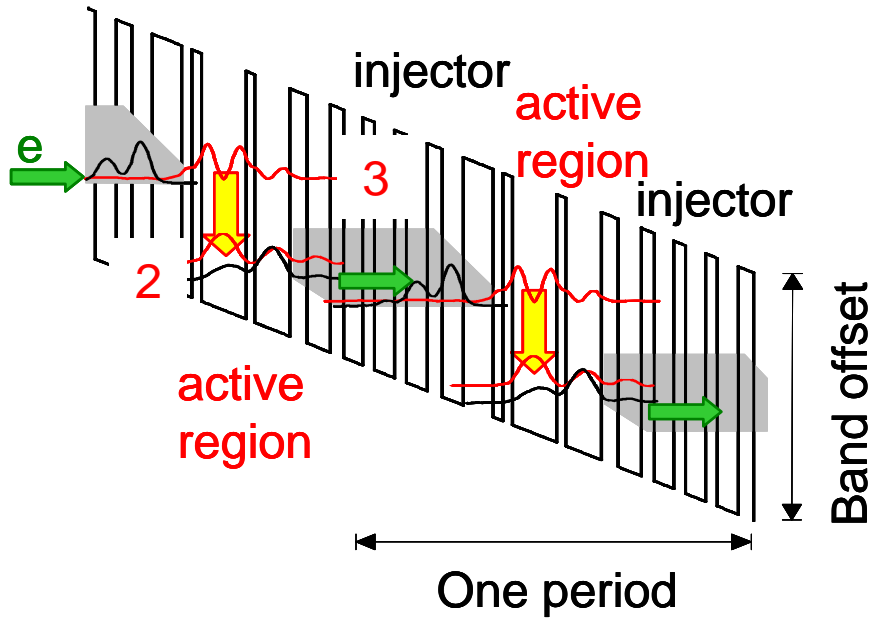
Fig. 2.2 Schematic of a QC laser, shown is an exemplary band structure consisting of alternating active regions and injectors. The green arrows indicate the flow of the charge carriers; the yellow arrows indicate the optical intersubband transition.

Quantum cascade lasers were first demonstrated in n-type InGaAs/AlInAs grown lattice matched to InP [1]. Currently, we notice a clear tendency to an increased family of materials systems, for example the inclusion of InGaAs in the GaAs/AlGaAs system [2], or luminescence measurements on Sb-based electronic structures [3], as well as p-type Si/SiGe based QC structures [4].

2.2 Timeline of Si-based QCL Research

The intersubband electroluminescence from silicon-based quantum cascade structure grown by MBE was first introduced in 2000 [4]. Two groups remain active in this field.

A Swiss-led group used a five quantum well active region — injector structure, grown on Si substrate, and with different Ge concentration in quantum

wells, designed to emit between heavy-hole subbands, to target electroluminescence around 10 μm wavelength. To cope with the excessive strain, the cascade was interleaved with thick Si layers repeatedly after few periods of active regions and injectors. The emission spectrum was strongly transverse magnetic polarized and slightly less than 20% of the peak energy broad and no optical gain was observed in this structure [4]. In 2004, the same group showed electroluminescence from a digital $Si/Si_{0.2}Ge_{0.8}$ multiple quantum well structure grown lattice matched to a $Si_{0.5}Ge_{0.5}$ pseudo-substrate [5]. The design was based on a so called "bound to continuum" approach between heavy-hole, sub- and minibands. A rather broad, but well-polarized emission was detected at around 7 μm wavelength. However, still no optical gain has been achieved.

A German-led research group reported on a seven quantum well design, again using different SiGe alloy compensation. Intersubband electroluminescence around 8.5 μm wavelength with rather broad (~20% of the peak energy) linewidth was demonstrated.

Recently, efforts are underway to develop THz QC lasers based on Si/SiGe [6]. THz emission at 2.9, 8.9 and 16.2 from a Si/SiGe superlattice has been reported [7].

2.3 Comparison Between Si-based and III-V Material Systems

Developing Si-based optoelectronics is one of the major breakthroughs expected for the coming decade. The expected advantages of Si-photonics include (i) cost effective, high-yield, large area manufacturing process that can be transferred from microelectronics to optoelectronics manufacturing, (ii) a considerable tighter integration between micro- and optoelectronics, and (iii) the high speed, larger

bandwidth, and lower power dissipation for microelectronics processors if on-chip communication is carried out by optical signals rather than metal vias and wires [8].

In addiction, Si has a higher thermal conductivity than GaAs, thus providing better thermal management, which is a key issue in any optoelectronic system. Silicon and SiGe alloys also have the advantage of a relatively large radiative-to-nonradiative branching ratio for the intersubband laser transition. In Si/SiGe heterostructures, the non-polar optical phonon scattering is weaker than the polar optical phonon scattering found in III-V heterostructures.

Unlike the conduction intersubband transitions employed in III-V QCLs, all current attempts to realize Si/SiGe quantum cascade lasers are based on valence intersubband transitions in p-type heterostructures. There are various reasons underneath it. For growth of pseudomorphic Si/SiGe heterostructures directly on silicon, substantial band offsets can only be achieved in the valence band. The standard method of obtaining usable conduction band offsets is to grow the heterostructure on a relaxed SiGe buffer (or virtual substrate). Even then the offsets obtained are generally not as large as those available in the valence band (up to 740 meV for pure Si on pure Ge [9]).

One disadvantage of the p-type SiGe system is that the hole masses are significantly larger than the III-V electron masses. Consequently, the hole wavefunctions in SiGe heterostructures are quite well localized in individual quantum wells, hence interwell coupling is weak. Therefore, delocalized superlattice type states cannot be formed unless the barrier layers are very thin. For the same reason, the device currents in p-SiGe QCLs will be lower than in III-V devices for the same external bias. Also, both heavy hole and light hole subbands are always present in p-

SiGe heterostructures, which is an added complication in the design of edge emitting laser based on heavy hole to heavy hole transitions.

Another difference between p-type Si/SiGe heterostructrues and n-type III-V systems appears in plots of subband energy versus the wavevector k_x and k_y (the in-plane dispersion). The valence subband dispersion are both anisotropic and non-parabolic, while the conduction subband dispersion in III-V materials are isotropic and almost parabolic (for the range of wavevectors typically encountered in cascade lasers). This feature of p-Si/SiGe system obviously complicates device design.

2.4 Practical Considerations in Si-based Systems

The realization of QCL in the Si-based material system is limited in practice by three practical considerations. These are inherent quality of the quantum wells, e.g. surface planarity, structural perfection, and the strain due to the lattice mismatch between the Si and the SiGe layers. The most significant issue in practice is the strain issue.

Surface (and interface) planarity is not an issue in conventional devices such as HBT's, but is of paramount importance for QCL. By lowering the growth rate compared to that which we would use for HBT's, we have been able to obtain extremely flat surfaces, with RMS roughnesses on the order of 0.5 nm or less. The lower temperature prevents the surface mobility of absorbed species, which is what typically enables islanding and roughness to occur in strained layer epitaxy.

The second main issue associate with layer quality is the structural perfection of the materials itself. This is perhaps best reflected by photoluminescence. The indirect nature of the Si/SiGe bandgap and weak strengths of optical transitions can be observed only in material of very high purity free of deep level traps. Despite intense effort, luminescence from band-edge states (as opposed to defects) was not observed

9

in SiGe thin films, and was first observed in SiGe quantum wells and superlattices grown at Princeton by Rapid Thermal Chemical Vapor Deposition (RTCVD) [10].

It is essential that all layers in a QCL stack must be grown pseudomorphically on top of one another, which may total over one micron thick, considering misfit dislocations at layer interfaces will introduce too many defects for devices. The well known limit of QCL possibilities on silicon is the large built-in strain between silicon and germanium (~4%). We will take two different approaches towards addressing this critical materials issue.

The first approach is the use of SiGeC alloys to reduce the strain, which will be primarily focused on devices with band offsets in the range of 200 meV, for devices emitting in the 10-micron region.   Princeton has pioneered the growth and electronic application of this area [11].

For QCLs that emit in the 3-5-micron range, SiGe layers with 60-70% Ge content will be required. To accommodate the strain in such structures, it will be necessary to grow strain symmetrized structures on a relaxed "SiGe buffer", where the virtual substrate has a lattice constant on the order of 30-40% Ge. Such layers are in principle easy to grow, but in practice are exceedingly rough, which limits the development of Si/SiGe QCLs.

Two specific technologies will be used to solve this problem. The first is based on an on-going collaboration between Amberwave Semiconductor, which is the leading commercial supplier of relaxed buffer to the semiconductor industry. The second approach will be the relaxation of strained SiGe islands which have been physically transferred to boronphosphorsilicate glass (BPSG) compliant substrates [12].

2.5 Summary

In this chapter, we have introduced the basics of quantum cascade lasers and reviewed the development of Si-based QCLs. The strength and weakness of Si-based material system compared to the conventional III-V material system has been discussed. Finally, some practical issues in realization of Si-based QCLs are presented and the relevant solutions have been proposed.

References

[1] J. Faist, F. Capasso, C. Sirtori, D. L. Sivco. A. L. Hutchinson, and A. Y. Cho, *Science* **264**, 553 (1994).

[2] L. R. Wilson, J. W. Cockburn, D. A. Carder, M. J. Steer, M. Hopkinson, C. K. Chia, R. Airey, and G. Hill, *Electron. Lett.* **37** 1292 (2001).

[3] C. Becker, I. Prevot, X. Marcadet, B. Vinter, and C. Sirtori, *Appl. Phys. Lett.* **78** 1029 (2001).

[4] G. Dehlinger, L. Diehl, U. Gennser, H. Sigg, J. Faist, K. Ensslin, D. Grützmacher, and E. Müller, *Science* **290** 2277 (2000).

[5] L. Diehl, S. Mentes, E. Mueller, D. Gruetzmacher, H. Sigg, U. Gennser, I. Sagnes, Y. Campidelli, O. Kermarrec, D. Bensahel, and J. Faist, *Appl. Phys. Lett*. **81** 4700 (2002).

[6] C. R. Pidgeon, P. Murzyn, J. P. R. Wells, I. V. Bradley, Z. Ikonic, R. W. Kelsall, P. Harrison, S. A. Lynch, D. J. Paul, D. D. Arnone, D. J. Robbins, D. Norris, and A. G. Cullis, *Physica E* **13** 904 (2002).

[7] r. Bates, S. A. Lynch, D. J. Paul, Z. Ikonic, R. W. Kelsall, P. Harrison, S. L. Liew, D. J. Norris, A. G. Cullis, W. R. Tribe, and D. D. Arnone, *Appl. Phys. Lett.* **83** 4092 (2003).

[8] D. J. Lockwood and L. Pavesi, *Silicon Photonics: Topics in Applied Physics* **94** 1 (2004)

[9] M. Rieger and P. Vogl, *Phys Rev B* 14276 (1983).

[10] J. C. Sturm, P. V. Schwartz, E. J. Prinz, and H. Manoharan, *J. Vac. Sci. Tech.* **B 9** 2011 (1991).

[11] M. S. Carroll and J. C. Sturm, *Appl. Phys. Lett* **81** 1225 (2002).

[12] H. Z. Yin, K. D. Hobart, and F. J. Kub, *Appl. Phys. Lett.* **84** (18) 3624 (2004)

CHAPTER 3

GROWTH AND CHRACTERIZATION OF ULTRA UNIFORM BORON-DOPED SI/SIGE MULTIPLE QUANTUM WELLS BY RTCVD

3.1 Introduction

The quantum cascade (QC) approach for infrared light emission relies only on intersubband transitions and not a direct band gap. Applied to the Si/SiGe material system, it offers an opportunity to develop electrically pumped Si-based light emitters and lasers [1-4]. At the heart of a typical QC structure is a series of doped quantum wells in which the optical transitions take place. Because the process depends on intersubband levels, sharp and planar interfaces and abrupt doping are more critical for QCLs compared to conventional devices, such as HBTs. Furthermore, achieving gain with a narrow linewidth demands extreme repeatability of the QW width and composition.

Growth of Si/SiGe multiple quantum wells (MQWs) by both MBE and CVD, characterized by SIMS, have been reported by several groups [5-7], but the well to well uniformity and surface planarity have not been studied in detail. In this chapter, we report the growth of boron-doped Si/SiGe MQW structures by rapid thermal chemical vapor deposition (RTCVD) optimized for interface abruptness, surface planarity, background doping, and well to well uniformity.

3.2 Design of Si/SiGe MQWs

3.2.1 Strained $Si_{1-x}Ge_x$ Alloys

Ge and Si have a lattice mismatch of about 4%, therefore the lattice constant perpendicular to the growth direction of the $Si_{1-x}Ge_x$ alloy can vary between the value

13

of Si and the value of the relaxed $Si_{1-x}Ge_x$ alloy determined by Vegard's law. If the $Si_{1-x}Ge_x$ alloy grows pseudomorphically on the silicon substrate, depicted in Fig. 3.1 [a], the lattice constant of the alloy will be compressed in the plane of the wafer to match the substrate and expand in the growth direction according to the Poisson ratio for the alloy film, resulting in strain energy stored film. For thin $Si_{1-x}Ge_x$ film on Si (100) substrates, it is energetically remain coherently strained.

However, if the film thickness is increased, the energy associated with strain increases, and above certain thickness it is energetically favorable for the material to release strain by incorporation misfit dislocation at the interface, as shown in Fig. 3.1 [b]. The thickness above which a strained film is likely to relax is called the critical thickness. There are several theories to calculate the critical thickness, among which Mathews and Blakeslee [9] and People and Bean [10] are the most commonly used. Fig. 3.2 shows the critical thickness for strained $Si_{1-x}Ge_x$ layers as varied with Ge content. This implies that only very thin defect-free $Si_{1-x}Ge_x$ layers can be epitaxially grown for device applications. However, dislocation-free strained layers of thicknesses above the critical thickness can be grown in a metastable state, where kinetic limitations prevent the structure from relaxing.

The strain in an epitaxially grown $Si_{1-x}Ge_x$ alloy has important consequences for the electronic band structure. In an unstrained $Si_{1-x}Ge_x$ alloy, the conduction band minima are silicon-like (i.e. six degenerate valleys in <100> direction) up to Ge content of about 80%. The bandgap reduction compared to pure Si is fairly small, as shown in Fig. 3.3 (dashed line). The strain in the alloy removed the six-fold degeneracy in the conduction band as well as the two-fold degeneracy between light and heavy hole in the valence band, resulting in a stronger bandgap reduction in the strained $Si_{1-x}Ge_x$ alloy, as depicted in Fig 3.3 [11].

a //

a ⊥

Ge$_x$Si$_{1-x}$ Epilayer

Silicon
Substrate

a$_s$

misfit accomodated by elastic strain

a$_o$

Ge$_x$Si$_{1-x}$ Epilayer

Silicon
Substrate

a$_s$

mismatch accomodated with misfit dislocations
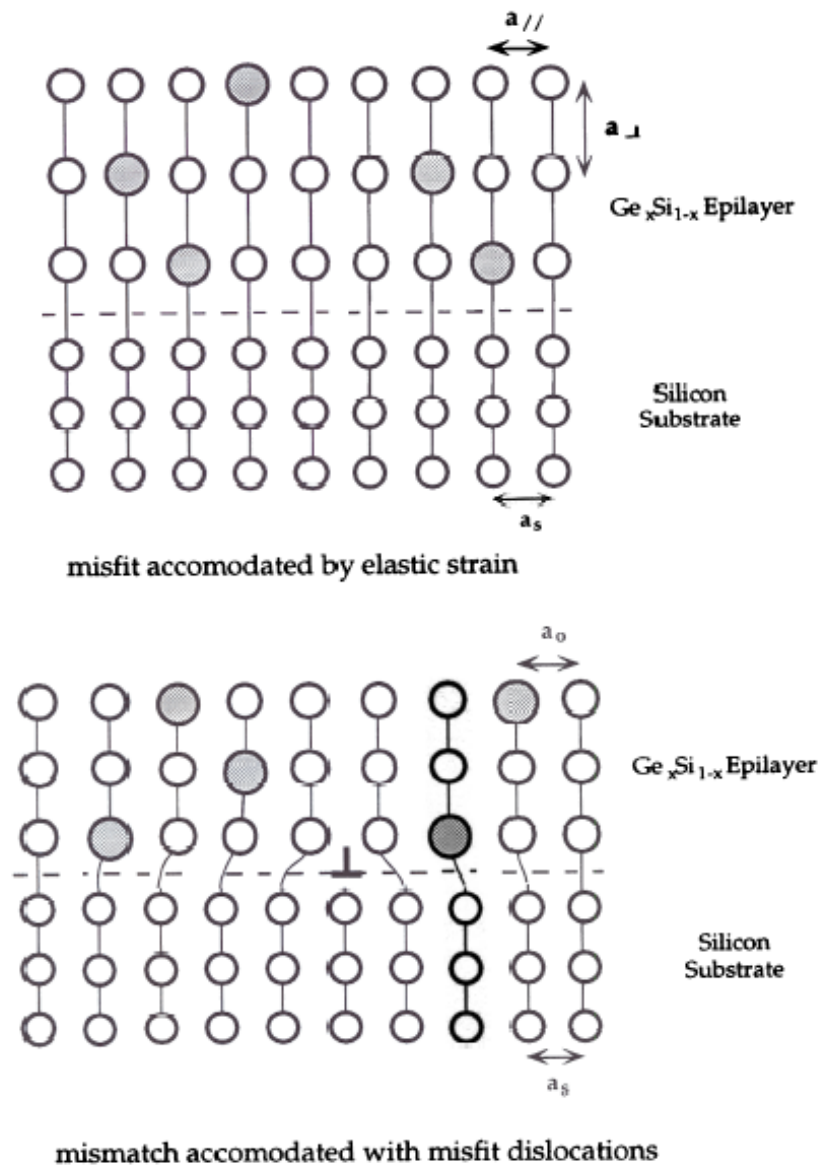
Fig. 3.1 Schematic showing two means of accommodating misfit, [a] formation of misfit dislocations and [b] epitaxial layer is coherently strained (adapted from [8]).
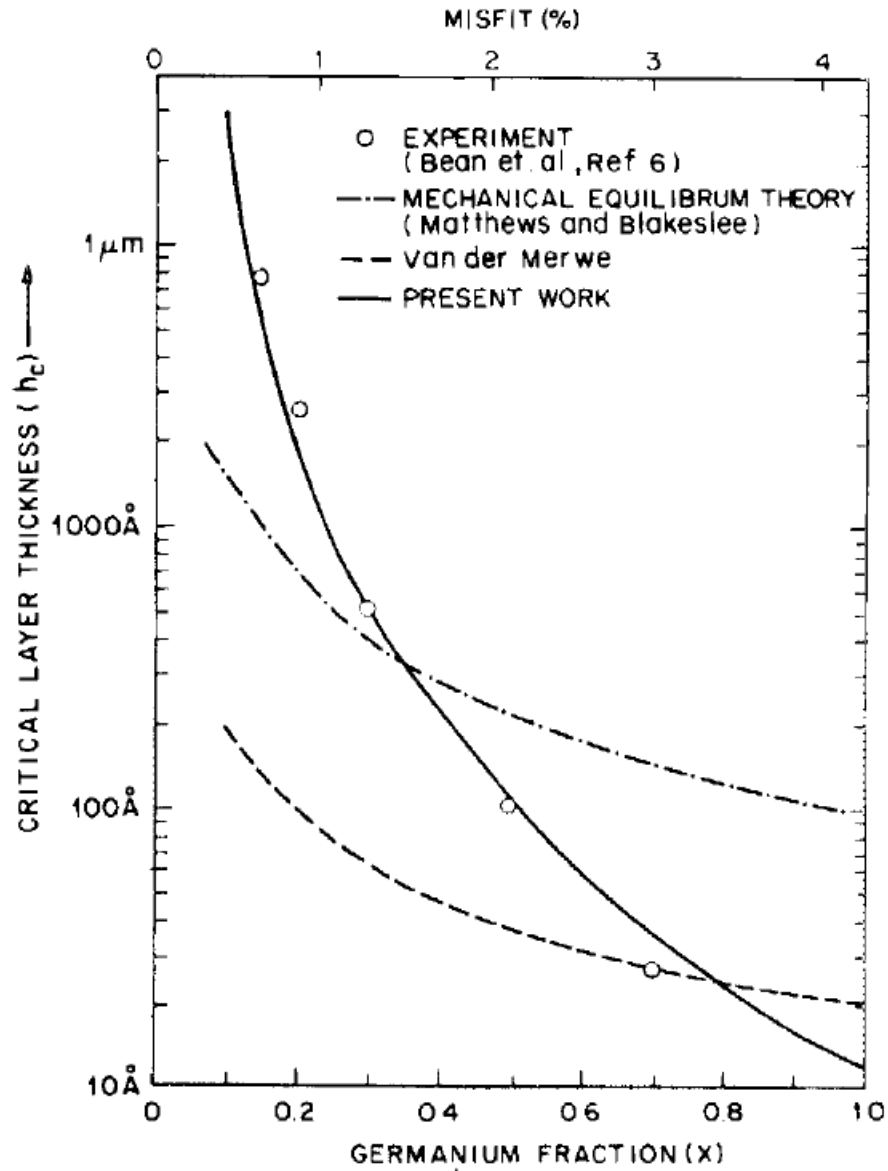
Fig. 3.2 Critical thickness of $Si_{1-x}Ge_x$ /Si heterostructure versus germanium fraction (adapted from [10]).
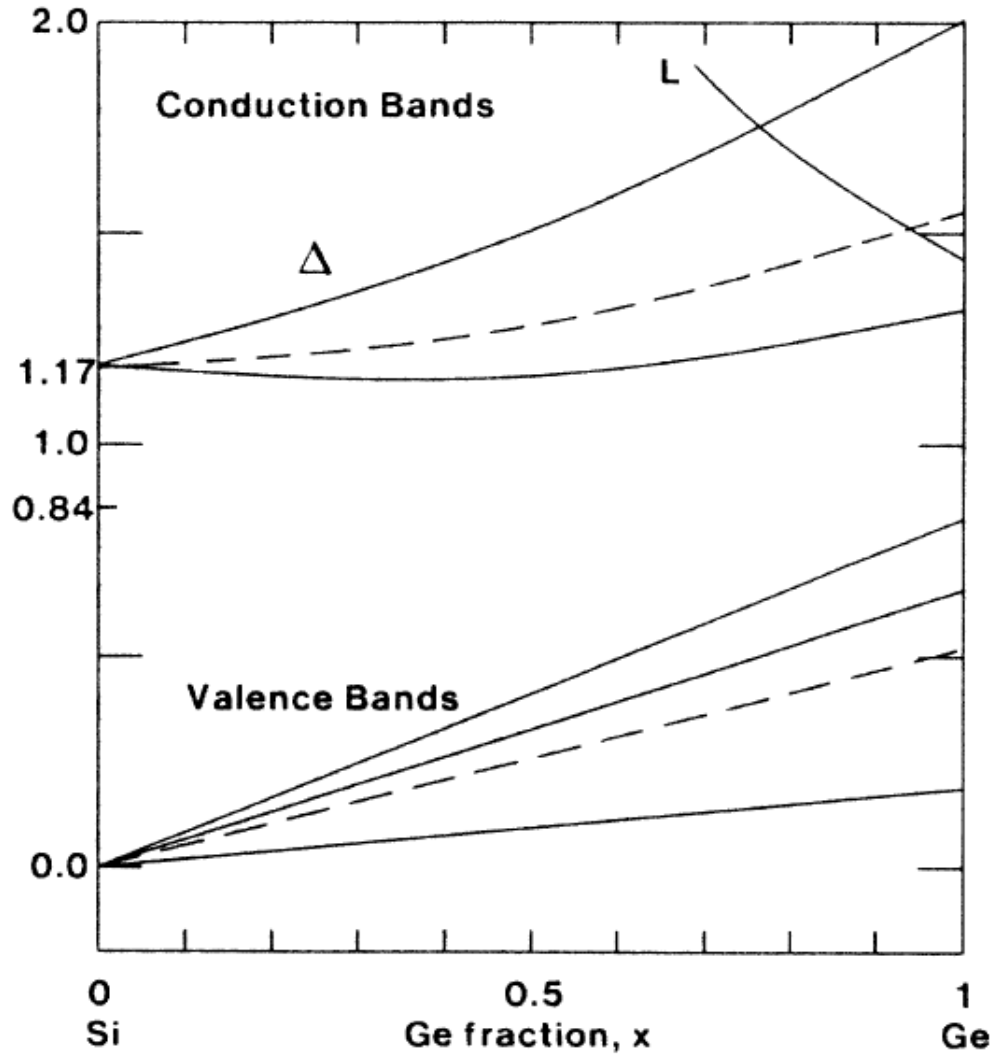
Fig. 3.3 Valence and conduction bands in strained $Si_{1-x}Ge_x$ alloys matched to a Si (001) substrate (adapted from [11]).

3.2.2 Structure Design of Si/SiGe MQWs

The band offset in $Si_{1-x}Ge_x$/Si (100) heterojunction is substantially in valence band, while the conduction band offset is minimal, as shown in Fig. 3.4. Therefore, the attempt of design of Si/SiGe MQWs for Mid-IR application can only be based on

p-type. The target band offset is around 250meV, which corresponds to a 35% Ge on Si.
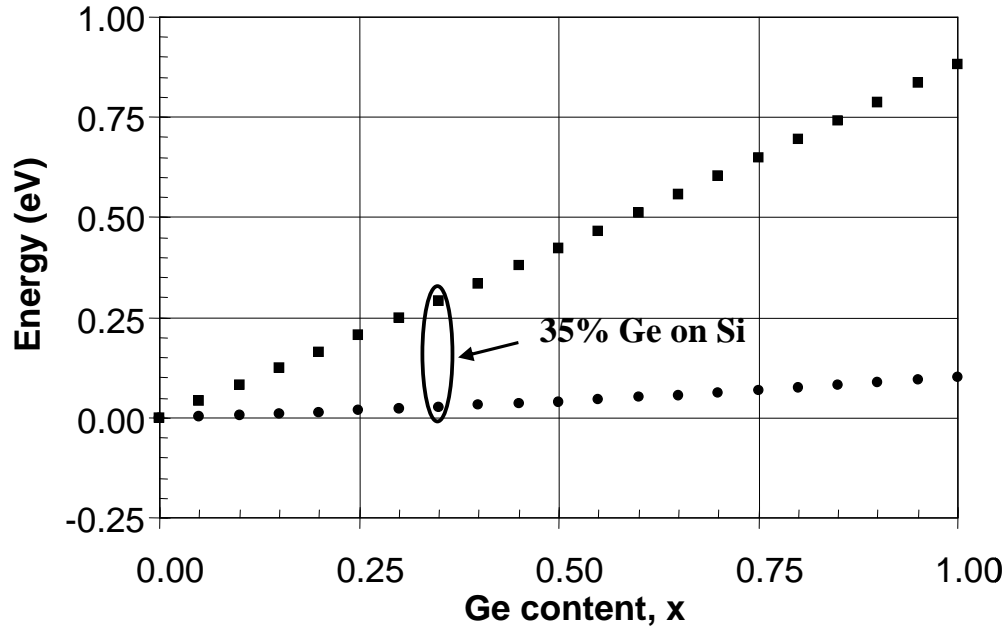
Fig. 3.4 Valence band offset as a function of Ge content in strained $Si_{1-x}Ge_x/Si(100)$.

. Fig. 3.5 displays the heavy hole energy levels for different $Si_{0.65}Ge_{0.35}/Si$ quantum wells, which is based on single quantum well and pure heavy hole energy band. The intersubband transition wavelength can be obtained by subtraction between two heavy hole states. An increase of interusbband transition wavelength with $Si_{0.65}Ge_{0.35}/Si$ quantum well width has been observed, i.e. 25 Å well width for 8.5 μm transition and 30 Å well width for 10.2 μm transition. For the quantum well width smaller than 20 Å, the energy level of HH_2 is no longer bounded in the quantum well. Fig. 3.5 shows the simulated valence-band states in a 25-Å quantum well with 35% Ge concentration, as well as the squared moduli of the envelope functions of the first four energy levels.
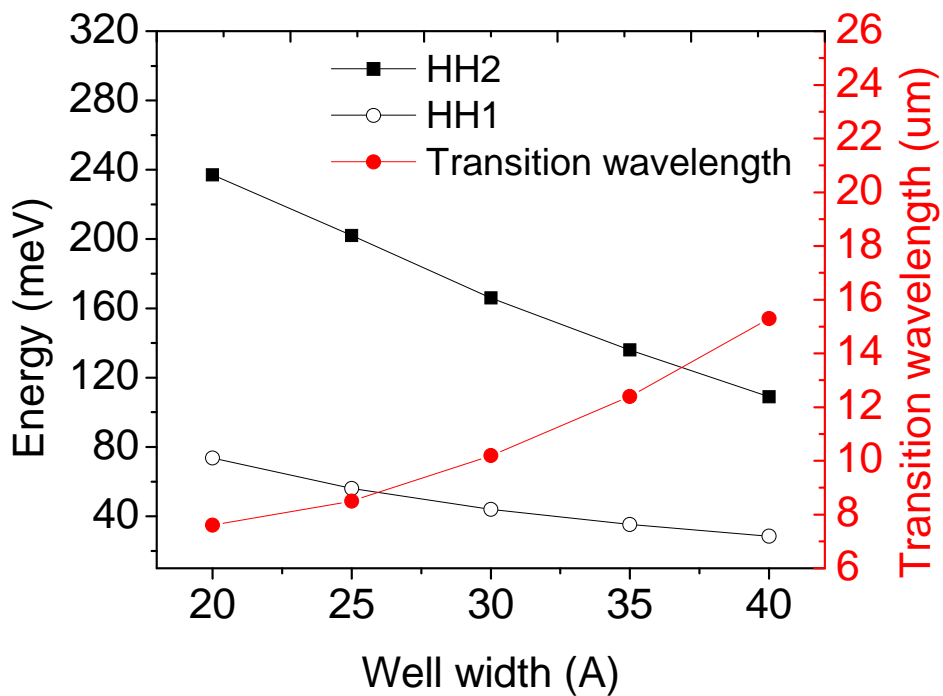
Fig. 3.5 Intersubband transition wavelength versus quantum well width.
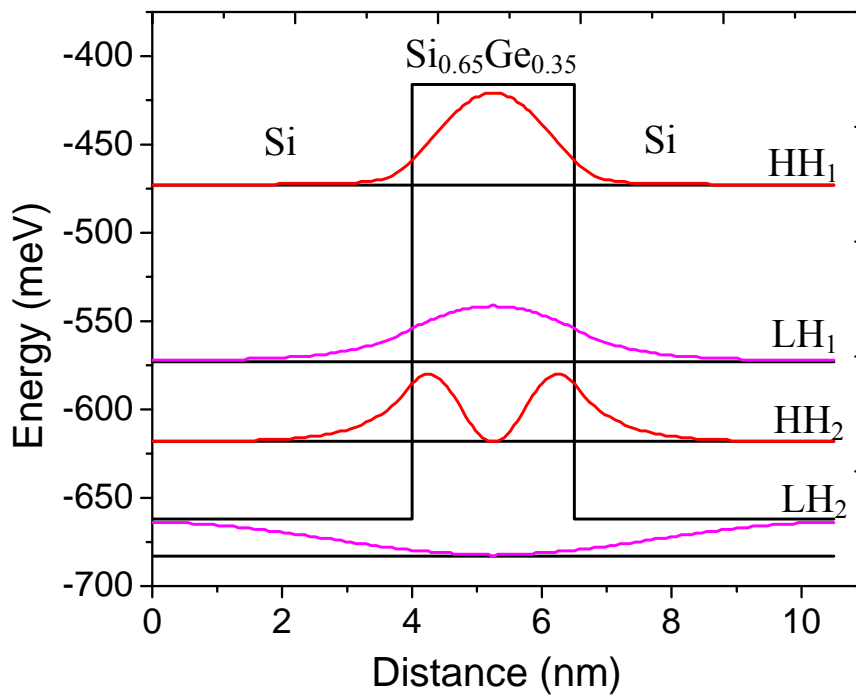
Fig. 3.6 Subands of valence-band $Si_{0.65}Ge_{0.35}$/Si (2.5nm/10nm) quantum well.

In the pseudomorphic growth of $Si_{0.65}Ge_{0.35}$ alloy on Si (100) substrate, the equilibrium critical thickness is about 40 nm. In case of $Si_{0.65}Ge_{0.35}$/Si multiple quantum wells, the thin $Si_{0.65}Ge_{0.35}$ quantum well is interleaved with relatively thick Si barriers, which reduces the effective Ge concentration within one period. The average composition in $Si_{0.65}Ge_{0.35}$/Si (2.5nm/10nm) is about 7%, resulting in ~3µm equilibrium critical thickness. The 15-period $Si_{0.65}Ge_{0.35}$/Si (2.5nm/10nm) multiple quantum wells is thus the final design.

3.3 Growth of Si/SiGe MQWs by RTCVD

3.3.1 Comparison of Background Doping Between SiH_4 and DCS Growth

The structures described in this thesis were grown by rapid thermal chemical vapor deposition (RTCVD) with *in situ* measurement of infrared transmission to measure temperature. A schematic of the reactor is shown in Fig. 3.7 [12], which consists of a 17.5 cm diameter cylindrical quartz tube. The wafer is heated by a bank of tungsten-halogen lamps which allows for rapid temperature switching. A feedback system controls the wafer temperature accurately to within a few degrees.

Fig. 3.7
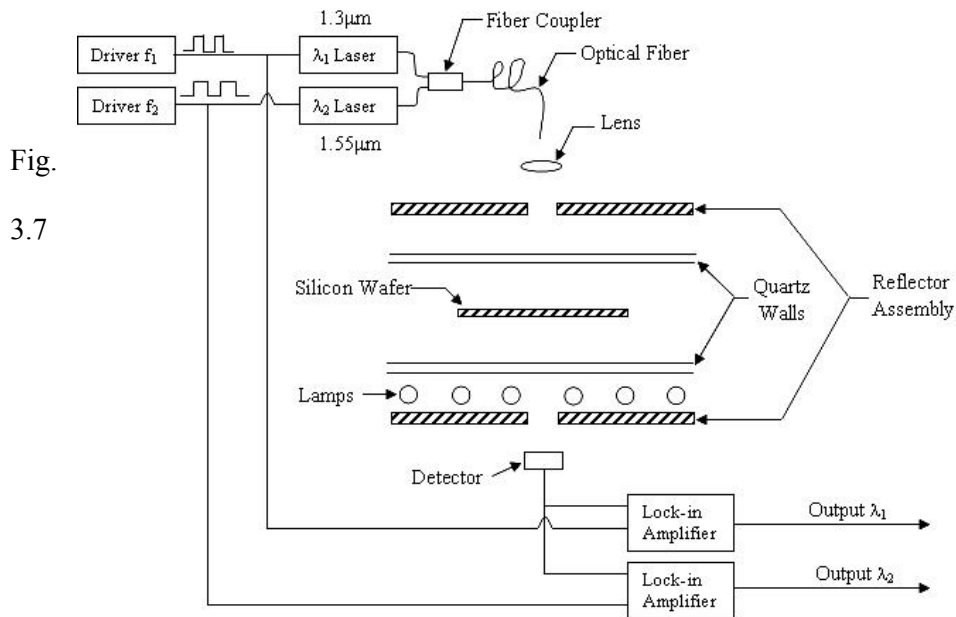
Schematic diagram of the rapid thermal processing adapted for infrared transmission measurements (Adapted from [12]).

The gases used are dichlorosilane (DCS) and silane (SiH_4) (10% SiH_4 in Ar) for Si and germane (0.8% GeH_4 in H_2) for germanium. The doping is accomplished simply by switching a diborane (10 ppm B_2H_6 in H_2) source on and off.

The wafers used for the experiments were 100-mm diameter boron-doped double-side-polished Si (100) wafers with a resistivity of ~10-20 Ω cm. The wafers were chemically cleaned using H_2SO_4 : H_2O_2 (30%) 1.5 : 1 for 15 min and followed by a dilute HF dip before loading into the chamber.

Low background doping is critical in QCLs to achieve a uniform electrical field, but due to the history of our reactor, RTCVD of SiGe with dichlorosilane as a silicon source (our usual choice) had high background phosphorous levels on the order of 10^{17} cm^{-3}. Fig. 3.8 shows the background phosphorous levels as a function of germanium concentration for both dichlorosilane and silane silicon sources. Silane-

based growth had acceptable phosphorous levels ($\sim 10^{16}$ cm^{-3}) compared to dichlorosilane-based growth and was used for the rest of the work in this thesis.
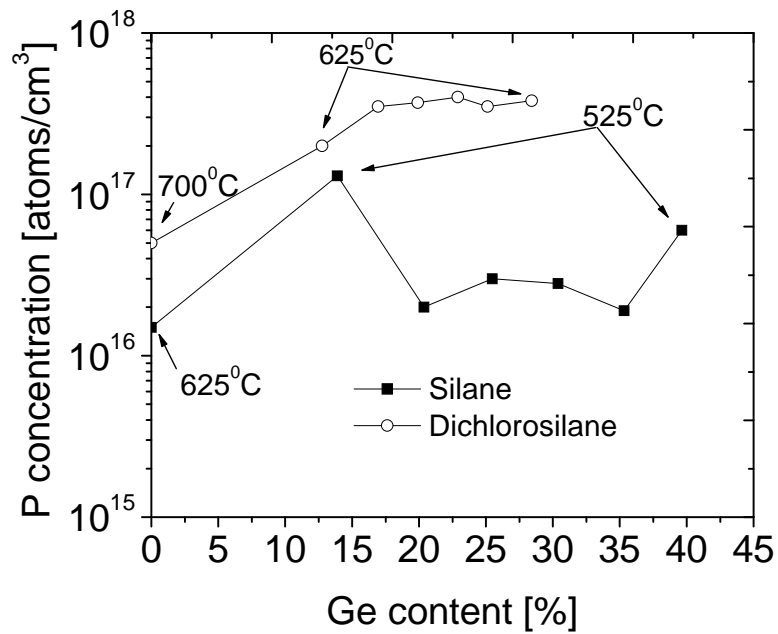
Fig. 3.8 N-type background doping for both silane and dichlorosilane silicon sources as a function of germanium content, the growth temperatures ranged from 525^{0}C to 700^{0}C, with growth pressure of 6 torr and a hydrogen carrier of 3 slpm. The silane flow was 10 sccm and the dichlorosilane flow was 6.5 sccm.

3.3.2 Calibration of SiGe Growth Condition

We now focused on the growth of boron-doped Si/SiGe multiple quantum wells with 15 periods to study hole intersubband transitions and infrared absorption and emission. Fig. 3.9 shows the growth rate and Ge concentration as a function of germane flow for conditions of 575⁰C and 525⁰C, respectively, with growth pressure of 6 torr, using a hydrogen carrier flow of 3 slpm and a silane flow of 10 sccm. As the germane flow is increased, both the Ge concentration and the growth rate increase. To achieve a sharp interface, we seek a low growth rate, on the order of ~0.1 nm/s. This is because of finite time to switch gases between layers and because a low growth rate is associated with a more planar interface [13]. Due to the higher growth rate of SiGe compared to Si, a temperature lower than the 625⁰C which is used for growth of Si is needed. The growth rate of SiGe at 575⁰C for 35% Ge (target for our work) is ~0.5 nm/s which is too high. Therefore we decreased the temperature to 525⁰C and achieved a growth rate of ~0.06 nm/s for 35% Ge.
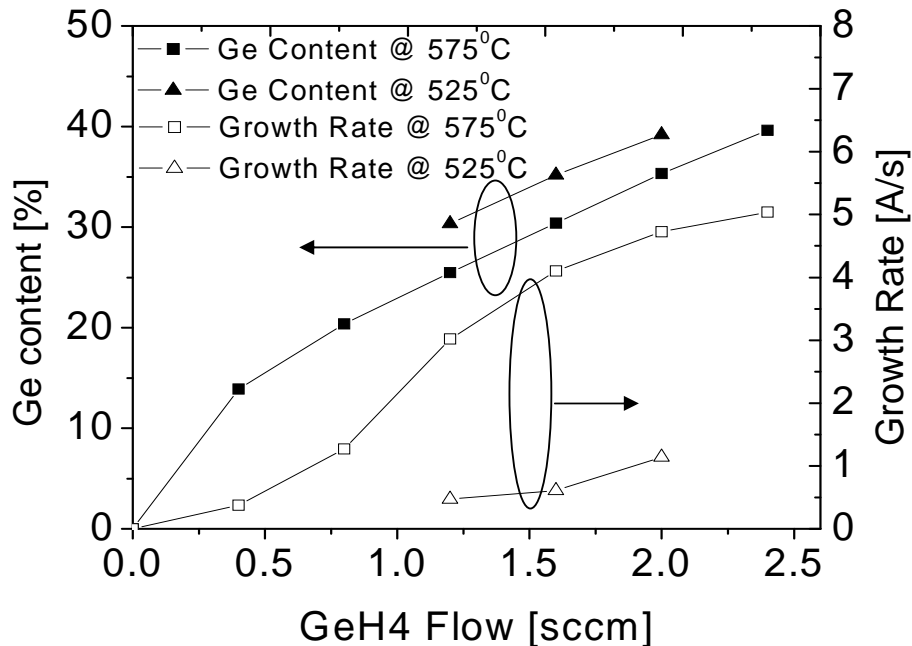
Fig. 3.9 Growth rate and Ge concentration versus germane flow rate using silane as a precursor at 525^0C and 575^0C. The pressure is 6 torr with a 3 slpm hydrogen carrier, and the silane flow is 10 sccm.

In growth, first an undoped Si 1-µm buffer layer is grown on the Si substrate. The multiple quantum well structure consists of 15 periods, each with a target of 2.5-nm-thick $Si_{0.65}Ge_{0.35}$ well and 10-nm-thick Si barrier (Fig. 3.10). The quantum wells are doped p-type with diborane varying from ~2×10^{18} cm^{-3} to ~3×10^{19} cm^{-3} in different samples. Within a single quantum well, the $Si_{0.65}Ge_{0.35}$ layer thickness of 2.5 nm compares to an equilibrium critical thickness of ~40 nm for a single such layer on Si(100). The average composition of the entire MQW structure of 2.5-nm-thick SiGe with 35% Ge is 7%, with a thickness of ~200 nm. This compares to an equilibrium critical thickness of ~3 µm for a single layer of 7% Ge [10].

| Si Cap 100 Å@625^0C |
| $Si_{0.65}Ge_{0.35}$ 25Å   B-doping ~10^{19}cm^{-3} @525^0C |

15 QWs

⋮

| Si 100 Å@625^0C |
| $Si_{0.65}Ge_{0.35}$ 25Å   B-doping ~10^{19}cm^{-3} @525^0C |
| Si Buffer ~ 1µm @1000^0C |
| <100> Si Substrate |
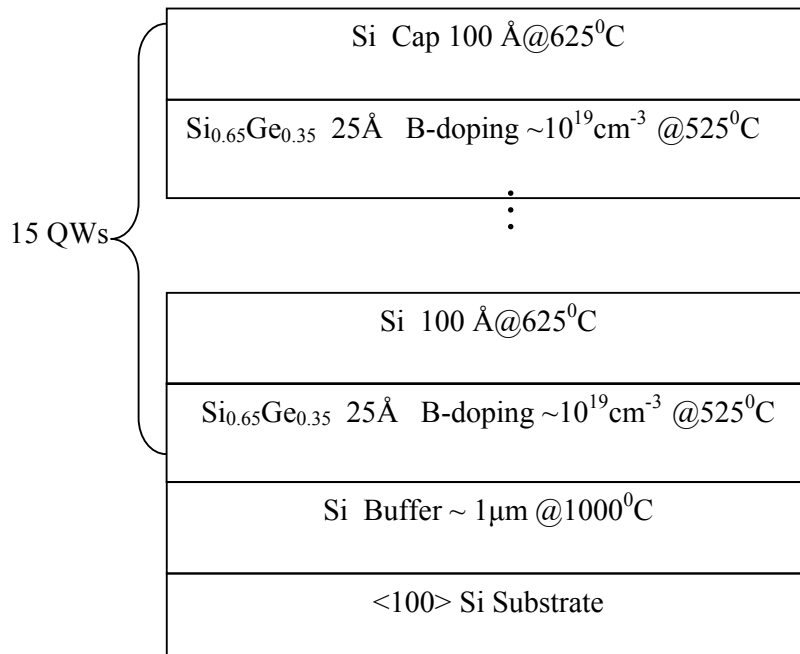
Fig. 3.10 Cross section of the targeted sample structure.

3.4 Characterization of Boron-doped Si/SiGe MQWs

3.4.1 High Resolution SIMS

The SIMS profiles were collected with a PHI mass spectrometer using a quadrupole mass detector. Both oxygen and cesium primary ion bombardment were performed, at low energy (less than 2keV). Positive and negative secondary ion detections were used.

The data were quantified using a SiGe reference material. The Ge concentration in the reference material was determined by both Rutherford Backscattering Spectrometry (RBS) and Auger Electron Spectroscopy (AES). The depth scales were determined by measuring the SIMS craters with a Dektak stylus profilometer. Corrections for the different sputter rates between the Si and SiGe layers were made.

High resolution SIMS measurements are shown in Fig. 3.11. The doping density profiles are extremely sharp (~2 nm/decade and ~3 nm/decade for the leading and trailing boron edges, respectively), with ~3 nm FWHM. These compare favorably to profiles of similar structure grown by UHV-CVD of ~3 nm/decade and ~6.5 nm/decade for the leading and trailing boron edges, respectively [7], although the results in all cases are affected by SIMS broadening effects.

As a quantitative test of well-to-well uniformity, Fig. 3.12 shows the period and the integrated areal density of boron and germanium in each quantum well. The middle 11 QWs show a nearly identical period of 18.2 nm with standard deviation about 0.1 nm (less than 1% of the period length). To the best of our knowledge, this reports one of the most uniform Si/SiGe MQWs reported to date. The growth interruption when switching between SiGe and Si was 30 s. To grow the entire MQW structure requires ~90 minutes. The uniformity implies the temperature varied less than 1^0C over the ~90 minutes of growth. The uniformity of the integrated B and Ge levels

per well was also excellent.

The drop in the period and integrated densities near the surface is thought to be a SIMS artifact. The rise of the FWHM of boron and germanium near the bottom of the QWs is an effect consistently observed in several samples. Whether this is a SIMS artifact or real effect is not clear.
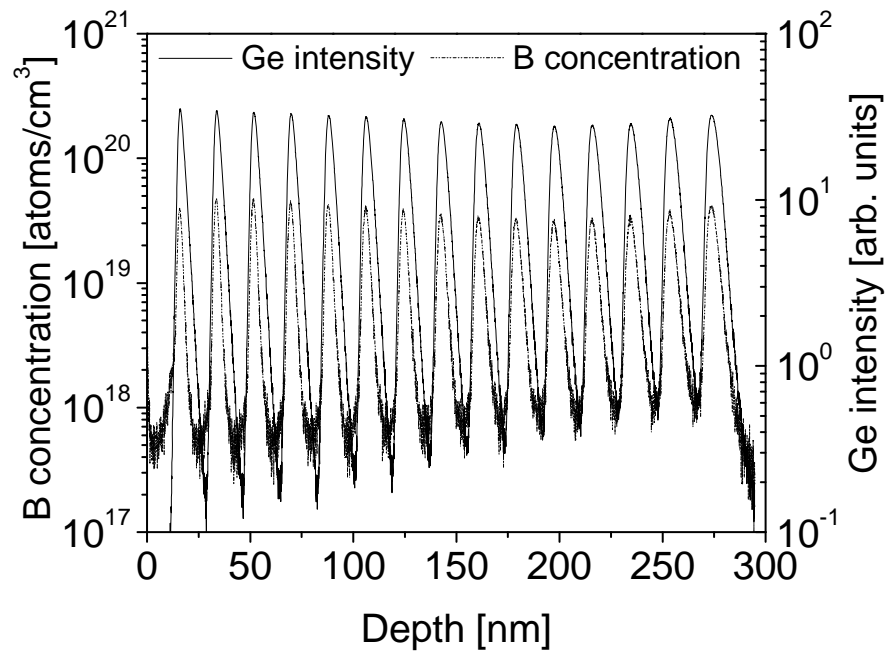
Fig. 3.11 SIMS profiles of Ge and B of the MQWs sample.
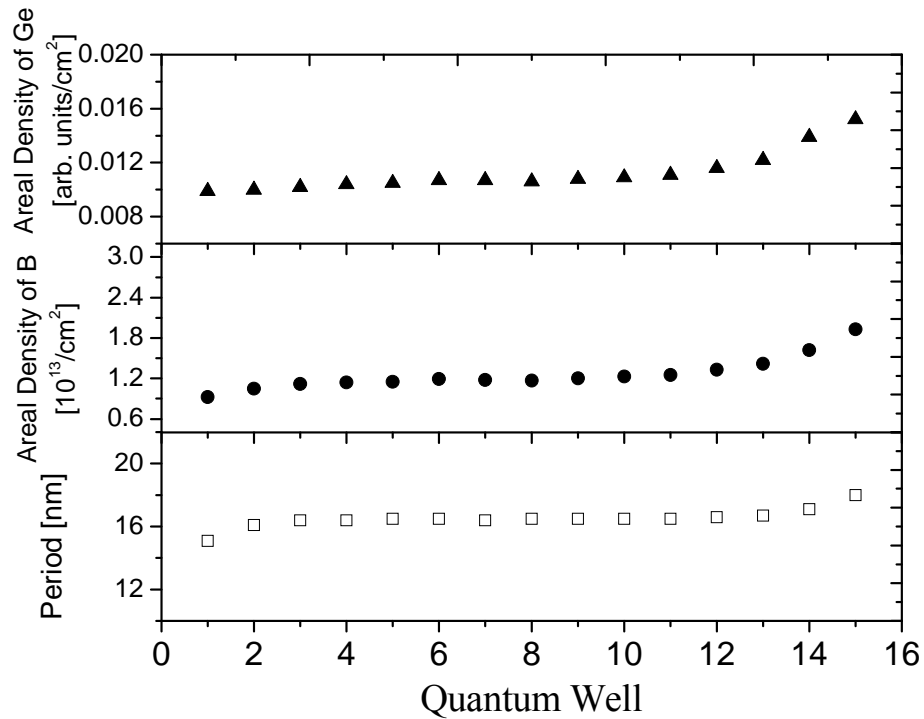
Fig. 3.12 The period and areal densities of B and Ge for each quantum well.

3.4.2 XTEM

Cross sectional transmission electron microscopy (XTEM) image of sample 3999 along [110] displays ultra uniform quantum wells with extremely good repeatability as shown in Fig. 3.13. The period of the Si/SiGe multiple quantum wells measured by XTEM is about 17nm which is consistent with the SIMS measurement. Fig. 3.14 shows the high resolution image of the Si/SiGe MQW structure. No dislocations and mismatches are found, showing good structural perfection. The measured quantum well width by HRXTEM was about 1.2 nm, only half of the target structure. The Si/SiGe interface is rather hazy which might own to the small contrast between Si and SiGe.
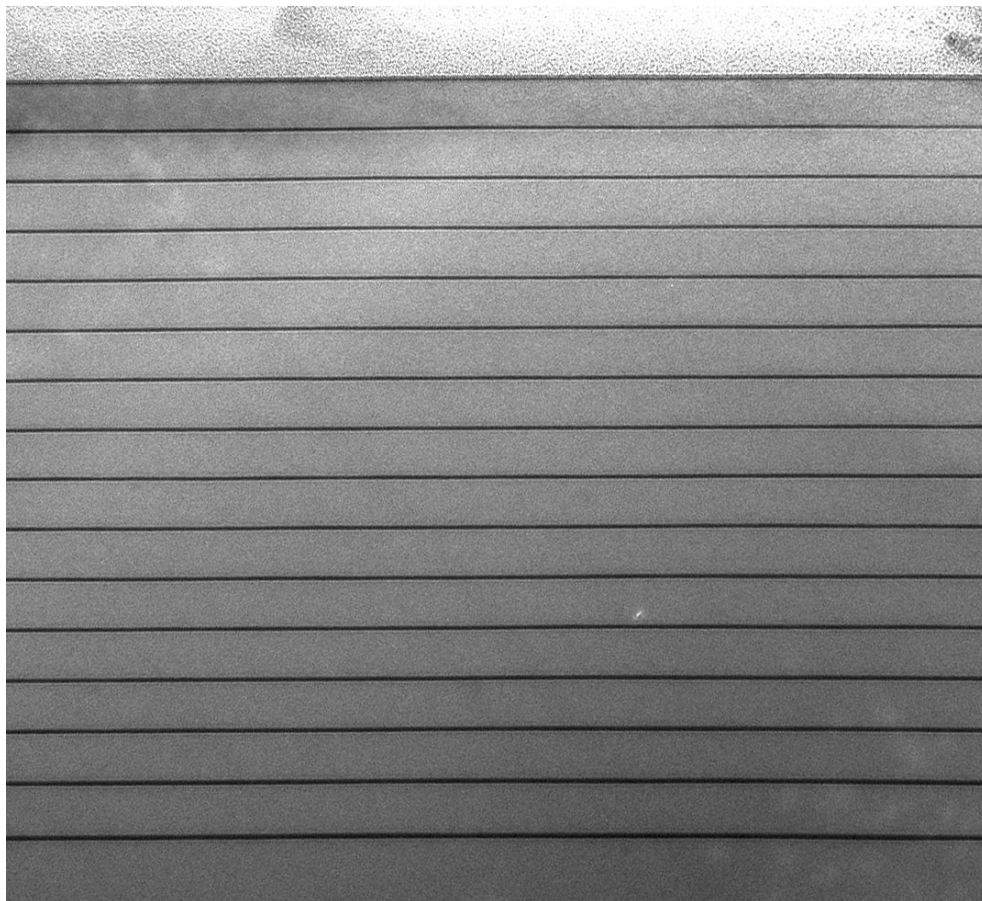
Fig. 3.13 XTEM image of sample 3999 showing entire 15 QWs.
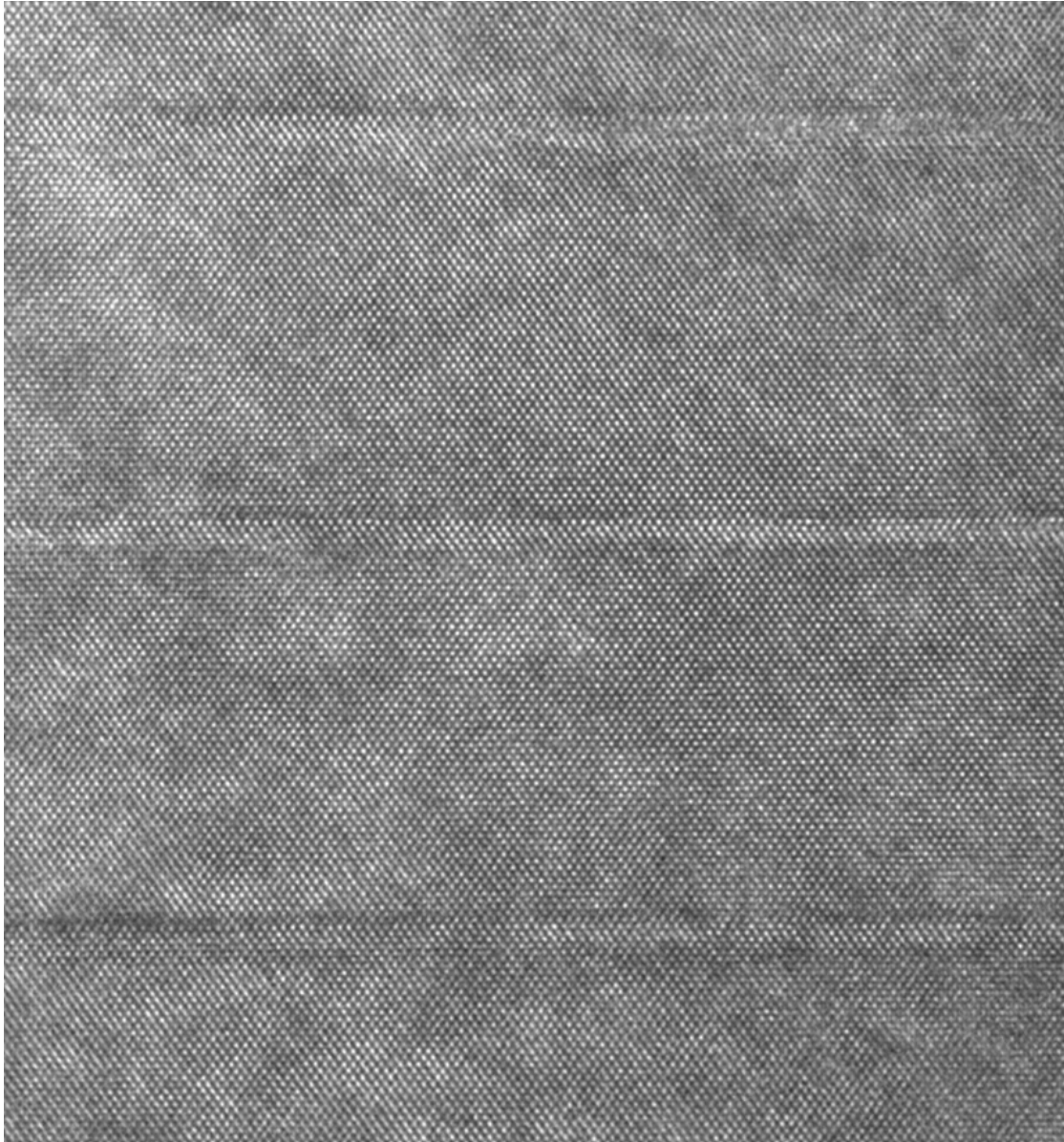
Fig. 3.14 High resolution XTEM image of sample 3999 showing atomic levels (380K×).

3.4.3 AFM

Surface and interface planarity is of paramount importance for QCLs, while it is not an issue for the conventional devices such as HBTs. We have examined the surface planarity in the structure of multiple quantum wells by AFM (Fig. 3.15). By lowering the growth rate compared to that which we would use for HBTs, we have been able to obtain extremely flat surface, with RMS roughness on the order of 0.2 nm or less. No SiGe islands have been observed. The lower temperature prevents the surface mobility of the absorbed species, which is what typically enables islanding and roughness to occur in strained layer epitaxy.

(a)

(b)

(c)

31
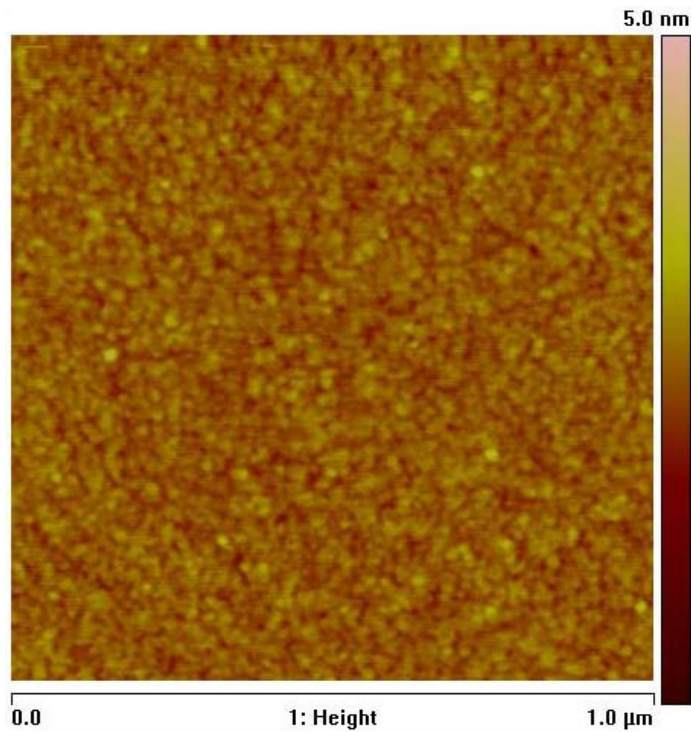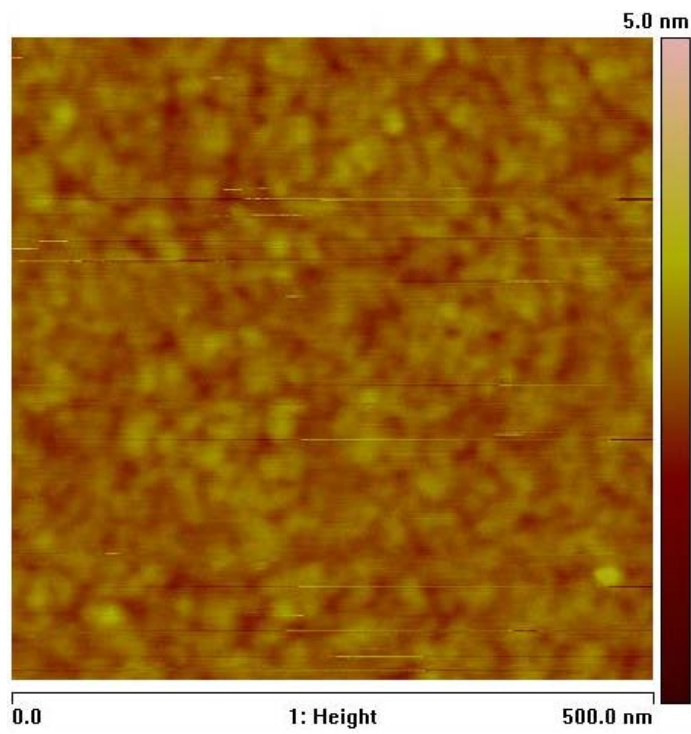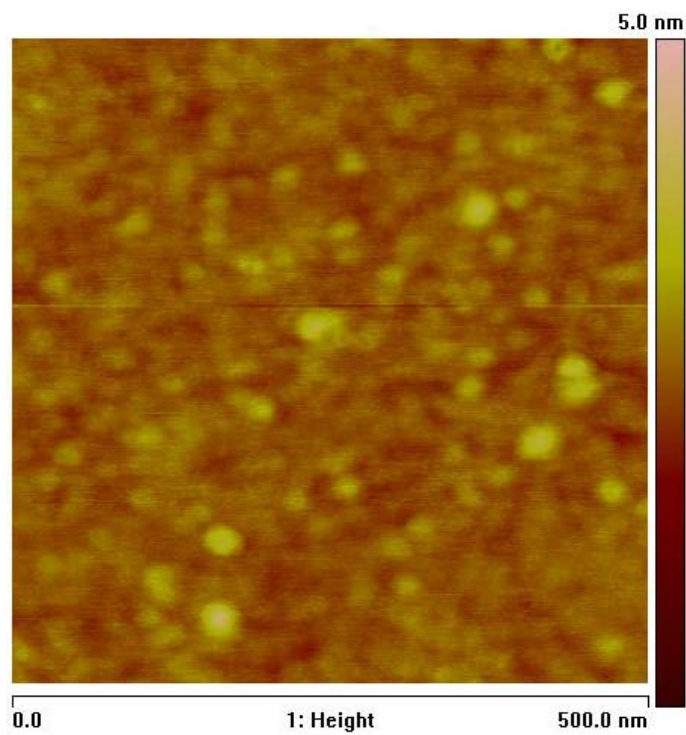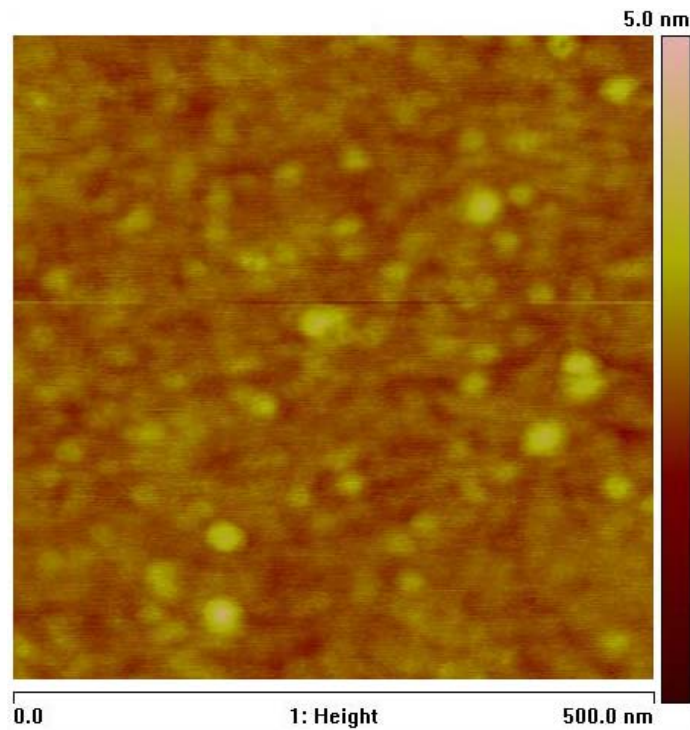
(d)

Fig. 3.15 Surface roughness measurement by AFM of (a) Si substrate, scale of 1 µm with rms of 0.2 nm; (b) Si substrate, scale of 500 nm; (c) MQW sample 3999, scale of 1 µm with rms of 0.18 nm; and (d) MQW sample 3999, scale of 500 nm.

3.4.4 XRD Simulation

In X-ray diffraction from thin layers, there will be two noticeable effects. First, there is expected peak broadening because there are not enough planes present to provide perfect cancellation around a diffraction peak. This effect becomes significant with layer thickness under ~1000 Å. Second, Pendellösung fringes might be visible around certain peaks. The layer thickness can be calculated from either of these phenomena. If we express the FWHM of a diffraction peak in angular units as $\Delta\omega$, then the thickness of the epilayer can be determined by Scherrer formula [14]:

$$t = 0.45\lambda/\Delta\omega\cos\theta$$

This effect is demonstrated in Fig. 3.16, which shows the simulated FWHM of the diffraction peaks from strained $Si_{0.8}Ge_{0.2}$ layers as a function of the epilayer thickness. The FWHM of the diffraction peaks demonstrate a reciprocal relation with the strained $Si_{0.8}Ge_{0.2}$ epilayers, decreasing monotonically with the epilayers.
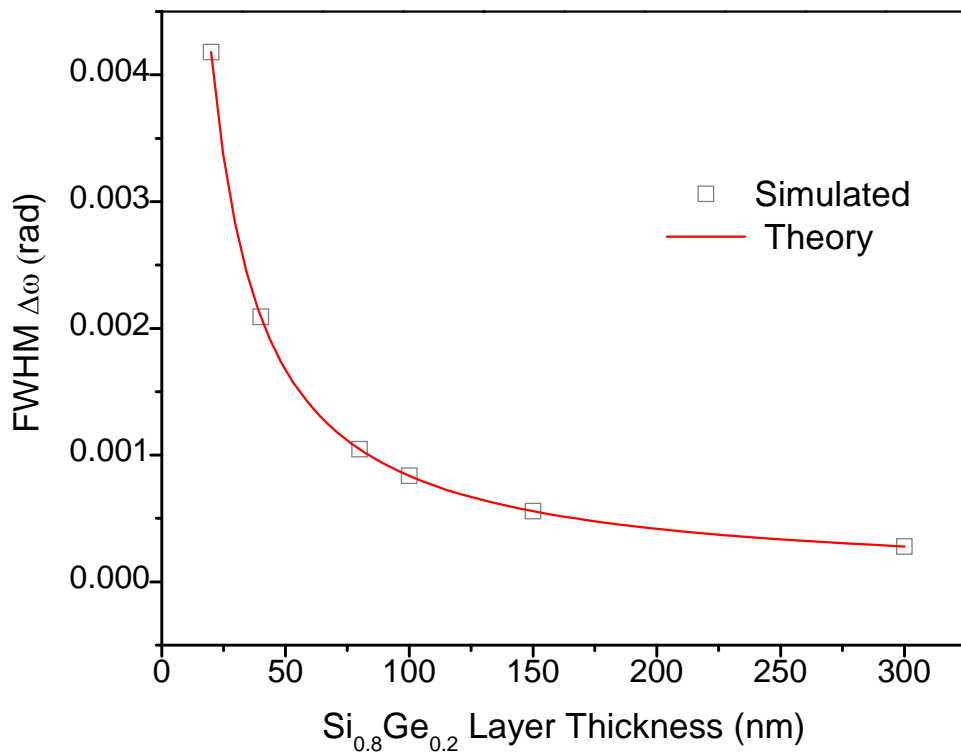
Fig. 3.16 Simulated FWHM of $Si_{0.8}Ge_{0.2}$ X-ray diffraction peaks versus strained $Si_{0.8}Ge_{0.2}$ epilayer thickness.

The effect of the Ge fraction on the position of the diffraction peaks both in strained and relaxed $Si_{1-x}Ge_x$ epilayers is simulated in Fig. 3.17. As shown, the $Si_{1-x}Ge_x$ diffraction peaks from both strained and relaxed epilayers normalized to the Si $K\alpha_1$ diffraction peak increase linearly with the Ge concentration. The slope from the

strained $Si_{1-x}Ge_x$ epilayers is steeper compared to that from the relaxed ones, which is in a good agreement with the theory.
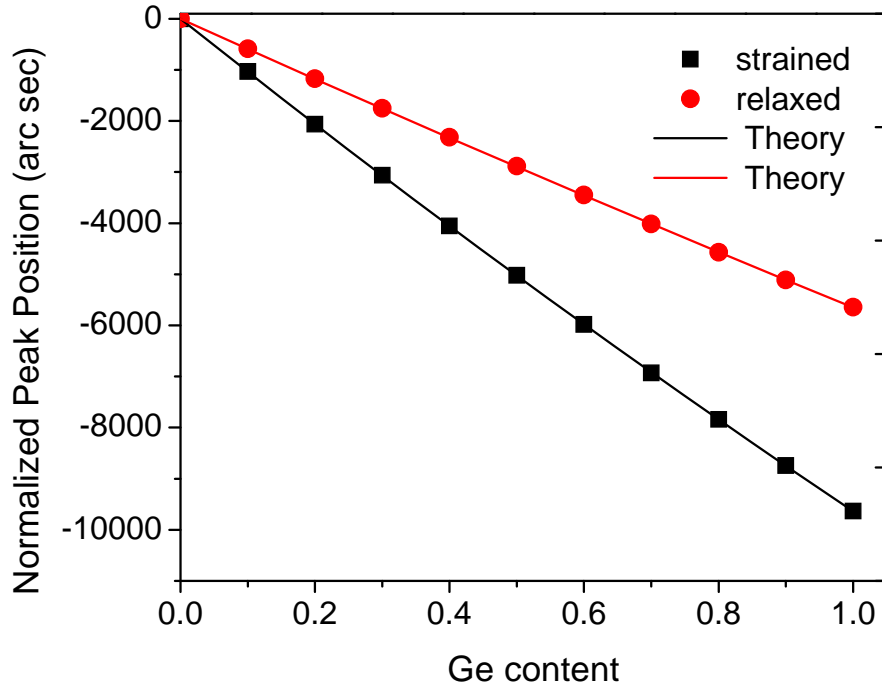
Fig. 3.17 Normalized peak position versus Ge fraction in single $Si_{1-x}Ge_x$/Si quantum well.

The X-ray diffraction pattern of superlattice typically shows a strong substrate peak, along with a series of satellite peaks, with which we can calculate the superlattice period and average superlattice composition as described below:

$$\Lambda = (i - j) \lambda / 2 (\sin\theta_i - \sin\theta_j)$$

Here Λ denotes the superlattice period and i and j means ith and jth order of the satellite peaks.

Fig. 3.18 depicts the simulation result of the satellite spacing between the nearest two satellite peaks versus the superlattice period. The simulation is based on 15-period $Si_{0.65}Ge_{0.35}/Si$ superlattice with varied period length. A monotonic decrease of satellite spacing with the period of the superlattice has been observed.
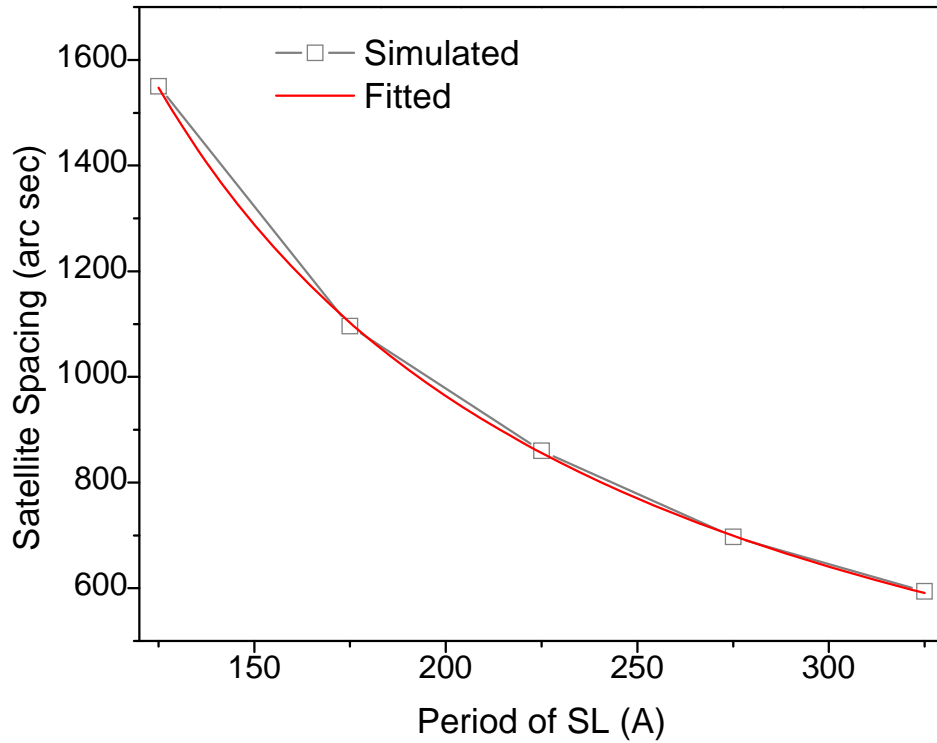
Fig. 3.18 Simulated satellite spacing as a function of period of $Si_{0.65}Ge_{0.35}/Si$ superlattice.

The interface mixing can be simulated by convoluting the Ge concentration profile of the quantum well with a graded interface, while conserving the relative Si and Ge amounts in the structure. Once the convolution is done, the lattice constants must be recomputed for each layer using the new concentration values. In order to simulate non-abrupt interface, we use four graded steps along both sides of the otherwise 25 Å-thick $Si_{0.65}Ge_{0.35}$ thin layer to demonstrate the interface broadening as shown in the inlet of Fig. 3.19. The effect of graded $Si_{0.65}Ge_{0.35}/Si$ interface region is

simulated for thin layers graded over 4 Ǻ, 8 Ǻ and 10 Ǻ, respectively. The simulated XRD spectra with abrupt and non-abrupt interface are almost identical, even for the fine fringe patterns. Therefore it might be difficult to determine the interface broadening of superlattice by X-ray diffraction.
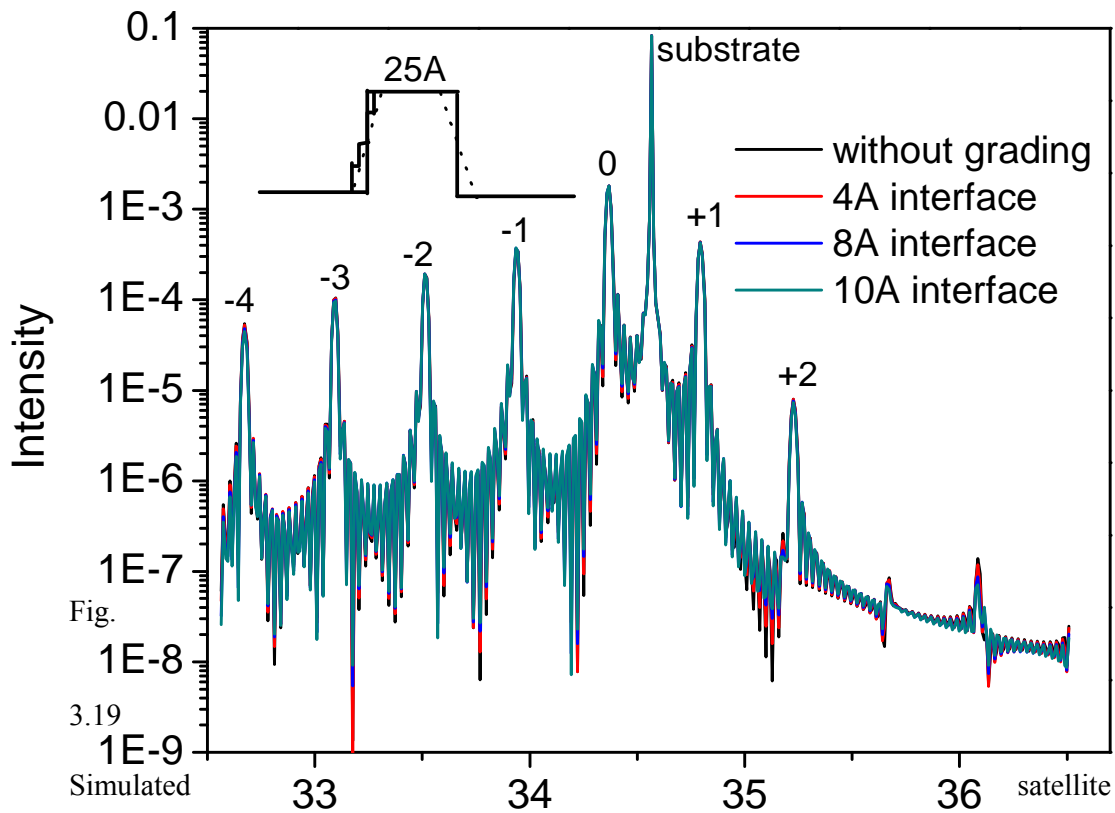
Fig. 3.19 Simulated peaks broadening of $Si_{0.65}Ge_{0.35}/Si$ (25Ǻ/100Ǻ) superlattice (15 periods) for various interface mixing.

3.5 Summary

We began this chapter with the design of the Si/SiGe multiple quantum wells in terms of valence band offset, quantum well width and number of periods of the superlattice.

We reported p-type Si/SiGe multiple quantum wells for intersubband transitions, grown by rapid thermal chemical vapor deposition with excellent well to well uniformity, as measured through high resolution secondary ion mass spectroscopy and high resolution cross sectional transmission electron microscopy. Critical factors are the use of a silane source for low background doping, the growth of the SiGe layer at a lower temperature to achieve a low growth rate, and repeatable temperature control.

Simulation of superlattice X-ray diffraction was performed to investigate the interface broadening. It is difficult to tell the interface mixing based on the simulation results.

References

[1] G. Dehlinger, L. Diehl, U. Gennser, H. Sigg, J. Faist, K. Ensslin, D. Grützmacher, and E. Müller, *Science* **290** 2277 (2000).

[2] L. Diehl, H. Sigg, G. Dehlinger, D. Grützmacher, E. Müller, U. Gennser, I. Sagnes, T. Fromherz, Y. Campidelli, and O. Kermarrec, *Appl. Phys. Lett.* **80**(18) 3274 (2002).

[3] L. Diehl, S. Mentese, E. Müller, D. Grützmacher, H. Sigg, U. Gennser, I. Sagnes, Y. Campidelli, O. Kermarrec, D. Bensahel, and J. Faist, *Appl. Phys. Lett.* **81**(25) 4700 (2002).

[4] I. Bormann, K. Brunner, S. Hackenbuchner, G. Zandler, G. Abstreiter, S. Schmult, and W. Wegscheider, *Appl. Phys. Lett.* **80**(13) 2260 (2002).

[5] H. Presting, J. Konle, M. Hepp, H. Kibbel, K. Thonke, R. Sauer, E. Corbin, and M. Jaros, *Opt. Eng.* **39**(10) 2624 (2000).

[6] P. Warren, M. Dutoit, P. Boucaud, J. M. Lourtioz, and F. H. Julien, *Thin Solid Films* **294** 125 (1997).

[7] R. Strong, R. Misra, D. W. Greve, and P. C. Zalm, *J. Appl. Phys.* **82**(10) 5191 (1997).

[8] E. J. Prize, PhD dissertation (1992).

[9] J. W. Matthews and A. E. Blakeslee, *J. Crystal Growth* **27** 118 (1974).

[10] R. People and J. C. Bean, *Appl. Phys. Lett.* **47** 322 (1985).

[11] C. G. Van de Walle and R. M. Martin, *Phys Rev B* **34** 5621 (1986).

[12] J. C. Sturm, P. V. Schwartz, E. J. Prinz, and H. Manoharan, *J. Vac. Sci. Technol.* B **9**(4) 2011 (1991).

[13] D. J. Robbins, A. G. Cullis, and A. J. Pidduck, *J. Vac. Sci. Technol.* B **9**(4) 2048 (1991).

[14] B. D. Cullity, Elements of X-ray Diffraction, Addison-Wesley, 1978.

CHAPTER 4

___

INFRARED STUDY OF SI/SIGE MQWS

4.1 Introduction

Two fundamental blocks for QC lasers are optical intersubband transition and transport through resonant tunneling [1]. Aside from complete QC laser structures, one can evaluate these two basic functions also individually, through intersubband absorption in doped, single and coupled quantum wells and through resonant tunneling diodes (RTDs), respectively.

To evaluate intersubband optical transition in absorption, suitably designed single or coupled quantum well structures are grown and doped such that the lowest energy level is populated. Broadband light is passed through the structure and transmission and absorption spectra are measured.

Another effective way to detect the intersubband transition is the photocurrent method. The incident photons are absorbed in discrete quantum wells that are normally much narrower than the inactive barrier regions, and photoemission occurs thereafter. The photocurrent caused by intersubband excitation will be discussed late in this chapter.

4.2 Transmission Measurement

4.2.1 Introduction

The specific nature of intersubband transitions — that is, the selection rule requiring an electric field component perpendicular to the QW layers — necessitates the use of nonstandard geometries to perform absorption experiments, which in turn require careful

consideration of the electromagnetics. To maximize it, we use a waveguide geometry. The samples were cleaved in strips and the cleaved edges were polished at 45° to provide multipass waveguide.

The absorption spectra were measured by the experimental setup in Fig. 4.1. The light from the internal IR source in Fourier transform infrared (FTIR) spectrometer is focused on the MQW sample edge by an off-axis parabolic mirror, after going through a polarizer and filtering out TE or TM polarized light. The incident light then undergoes a multipass waveguide, passes through a lens system, and is eventually collected by the detector, where the detected signal is magnified by a preamplifier and feed back to the FTIR.

The absorbance for polarization parallel to the plane of the layers is subtracted from the absorbance normal to the plane of the layer, to remove instrumental, substrate, and free-carrier contribution. Following is the detailed deduction of the intersubband absorbance.

$$I_{out} = I_{in}T_1T_2 \exp[-(\alpha_{iSB-TM} + \alpha_{iSB-TE} + \alpha_{fc} + \alpha_{imp} + \alpha_{scat})L_{eff}] \qquad (1)$$

where, I_{in} and I_{out} are the intensity for the incident and transmitted light. T_1 and T_2 are the transmission at both edges of the sample facets. α_{iSB-TM}, α_{iSB-TE}, α_{fc}, α_{imp} and α_{scat} are the absorption coefficient for TM-polarized intersubband, TE-polarized intersubband, free carrier, impurity and scattering absorbance. To simplify the equation, we denominate ($\alpha_{fc} + \alpha_{imp} + \alpha_{scat}$) as α_{other}. L_{eff} denotes the effective length of the optical path.

$$I_{out-TM} = I_{in-TM}T_1T_2 \exp[-(\alpha_{iSB-TM} + \alpha_{other})L_{eff}] \qquad (2)$$

$$I_{out-TE} = I_{in-TE}T_1T_2 \exp[-(\alpha_{iSB-TE} + \alpha_{other})L_{eff}] \qquad (3)$$

We first take natural logarithm of both sides of the above equations, then subtract Eq (2) from Eq (3) and get the final equation:

$$(\alpha_{iSB-TM} - \alpha_{iSB-TE})L_{eff} = \ln\frac{I_{in-TM}}{I_{in-TE}} - \ln\frac{I_{out-TM}}{I_{out-TE}} \qquad (4)$$

The absorption contribution from the instrument, the substrate, the impurity and the free carrier has therefore been removed.
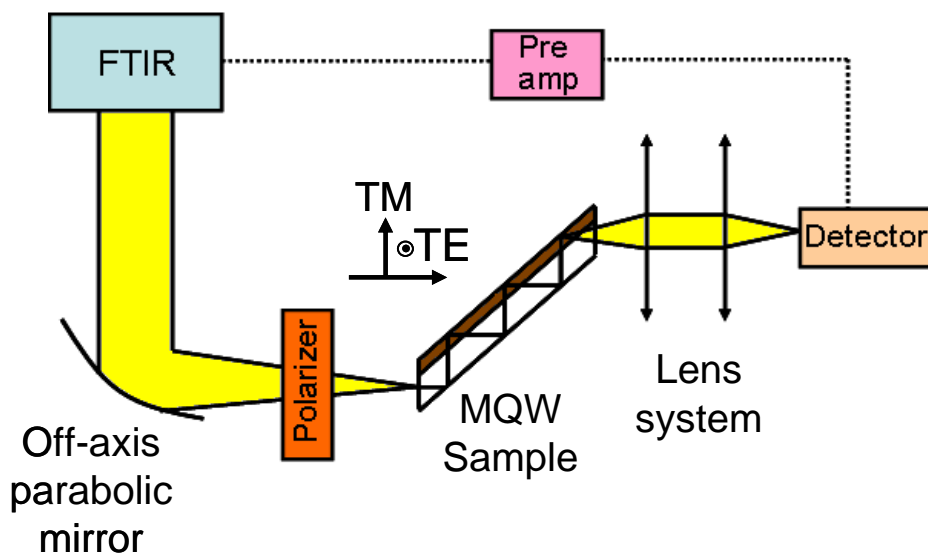
Fig. 4.1 Schematic diagram of multi-pass transmission measurements.

4.2.2 Intersubband Transition Measurement in InGaAs/AlInAs/InP QCL

The mid-infrared absorption measurements of QCL sample D2986 were done in a multipass waveguide geometry at temperature of 77 K and 300 K using the temperature controlled cold-finger of a liquid-nitrogen-flow cryostat. The spectra were taken with a Nicolet Fourier transform infrared spectrometer equipped with a cooled HgCdTe detector in rapid scan and the signal was averaged over 50 scans.

Fig. 4.2 shows the absorption spectra of out-of-plane (TM) subtracted by that of in-plane (TE) at 77 K and 300 K. As expected, the spectra exhibit three absorption peaks, corresponding to intersubband transition between E_4 to E_{18} (peak A), E_2 to E_{16} (peak B) and E_4 to E_{16} (peak C), respectively (shown in Fig. 4.3). The broader

absorption features measured at 300 K compared to those at 77 K are due to wider carrier distribution at higher temperature. The red shift of the absorption peaks at 300 K is likely due to the shrink of the band offset as the temperature increases.

The designed and measured energy values for the three intersubband absorption peaks are tabulated in Table 4.1. For peak A, the experimental data are in perfect agreement with the initial design, while peak B and C are within reasonable errors, about 15% and 25%, respectively.
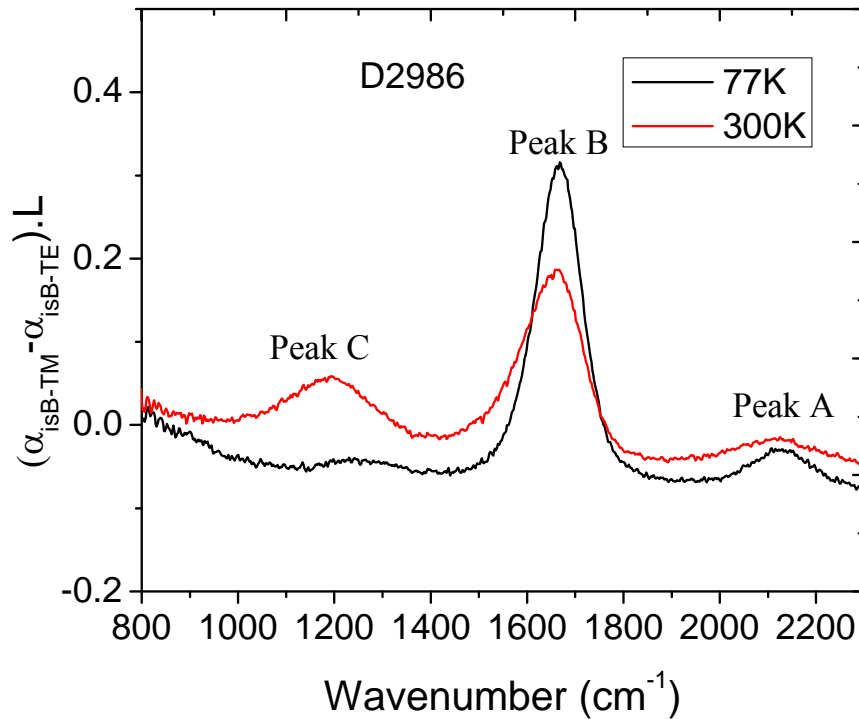
Fig. 4.2 Intersubband absorptions of QCL sample D2986 at various temperatures.
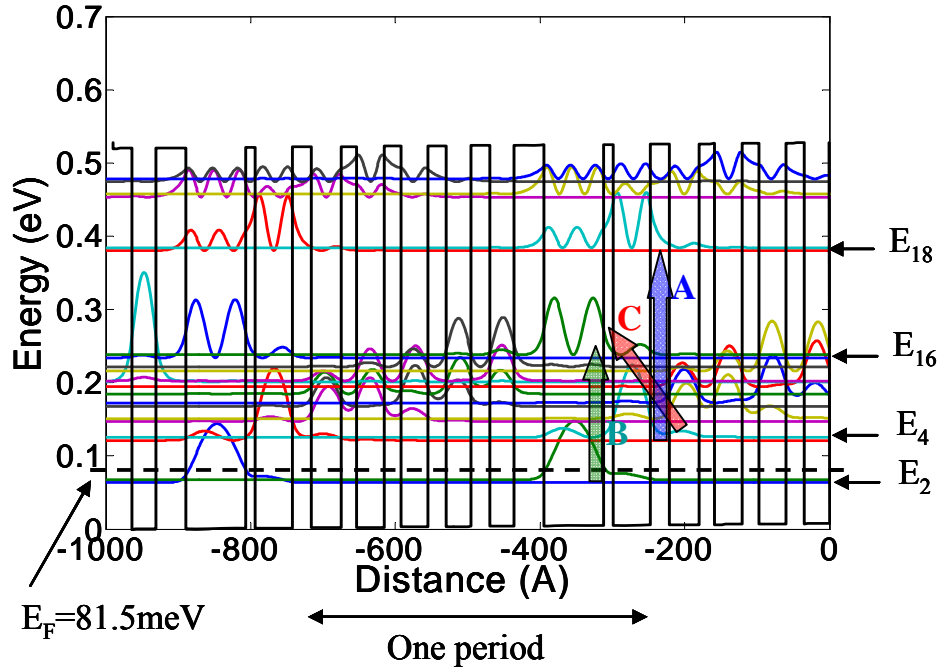
Fig. 4.3 Band structure of QCL sample D2986.

Peak	Designed Value (meV)	@77K	@300K
A	260.1 (E_4 to E_{18})	261.4	260.7
B	175.2 (E_2 to E_{16})	206.8	205.6
C	117.4 (E_4 to E_{16})	152.6	147.7

Table 4.1 Design and measured intersubband transition peaks of QCL sample D2986.

Note the sample is measured at two different temperatures.

4.2.3 Intersubband Transition Measurement in Si/SiGe MQWs

So far we have considered only intersubband transitions of electrons in the conduction band of quantum wells. In a similar way, of course, valence band intersubband transitions can be observed in quantum wells that are p-type doped. The main difference arises from the complexity of the valence band, which makes

reasonably accurate calculations significantly more difficult. We have discussed before that the main intersubband absorption occurs for an electromagnetic wave polarized along the growth direction (i.e., perpendicular to the layer planes). This selection rule holds very well for many cases (such as, e.g. a typical InGaAs QW), but there are several mechanism that can lead to relaxing this rule. Strong normal-incidence intersubband absorption has been predicted and observed for holes in valence-band quantum wells [2], which is due to the mixing of the various hole bands. In this section, we still focus on in-plane absorption in p-type Si/SiGe MQWs.

The absorption spectrum of a p-type doped $Si_{0.65}Ge_{0.35}/Si$ (25Å/100Å, $2\times10^{19}cm^{-3}$) multiquantum well structure is shown in Fig. 4.4 (b), with a reference of p-type doped Si substrate (Fig. 4.4 (a)). The main absorption feature is the strong peak centered at 1106 cm^{-1} (~1050 cm^{-1} and 1200 cm^{-1} absorption edges, respectively). Noting that this peak is also observed from the Si substrate, it is difficult to resolve the expected intersubband absorption peak designed at 1170 cm^{-1}, even though this feature exists. To avoid this complexity, we grew several other samples with different quantum well widths (e.g. 30Å), still the only strong absorption peak obtained is at 1106 cm^{-1}. We therefore doubt this peak might be irrelevant with the intersubband transition of the quantum wells. Several other absorption peaks are found below 1000 cm^{-1} with a few shoulder peaks. Those peaks will be identified in the next session.

(a)

(b)
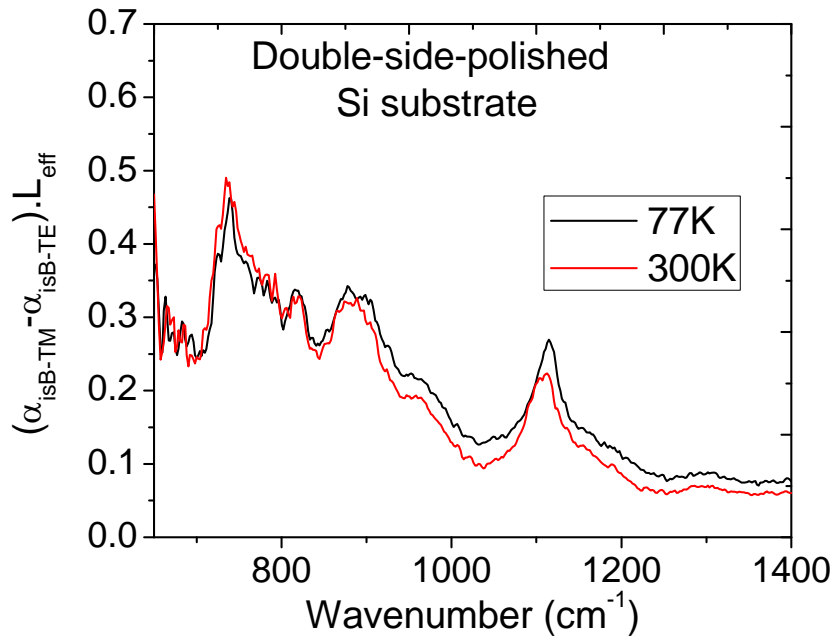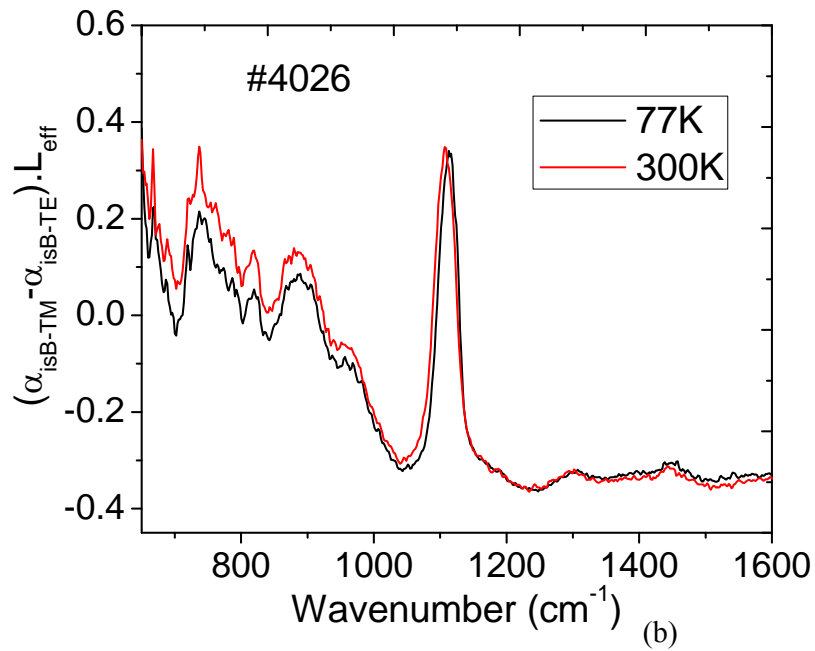
(b)

Fig. 4.4 Absorption spectrum of (a) Si substrate, (b) Sample 4026, at different temperatures.

4.2.4 Investigation of Interstitial Oxygen

The absorption spectra, measured by single-pass method, for sample 4026 and float-zone Si substrate are overlapped within the same figure, as shown in Fig. 4.5. We scaled the spectrum of float-zone Si in order to fit the peaks in the sample and found out that the strong absorption peak centered at 1106 cm^{-1} is attributed to the interstitial oxygen absorption superimposed with the three phonon absorption (TO+TO+TA). Meanwhile the absorption band below 1100 cm^{-1} is from either two-phonon-process absorption or three-phonon-process absorption as denoted in the figure.
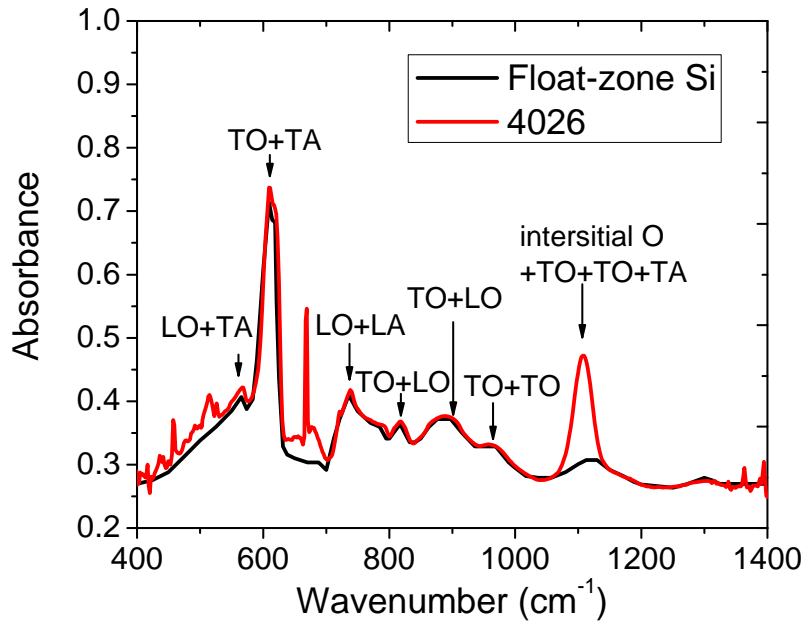
Fig. 4.5 Absorption spectrum of float-zone Si and sample 4026 by single-pass transmission measurements.

By subtracting the three-phonon absorption (centered at 1107 cm^{-1}) from the absorption spectrum of sample 4026, one can identify the main feature of the

interstitial oxygen absorption (Fig. 4.6), which is much sharper and stronger than the three-phonon absorption. The FWHM is about 32 cm^{-1}.
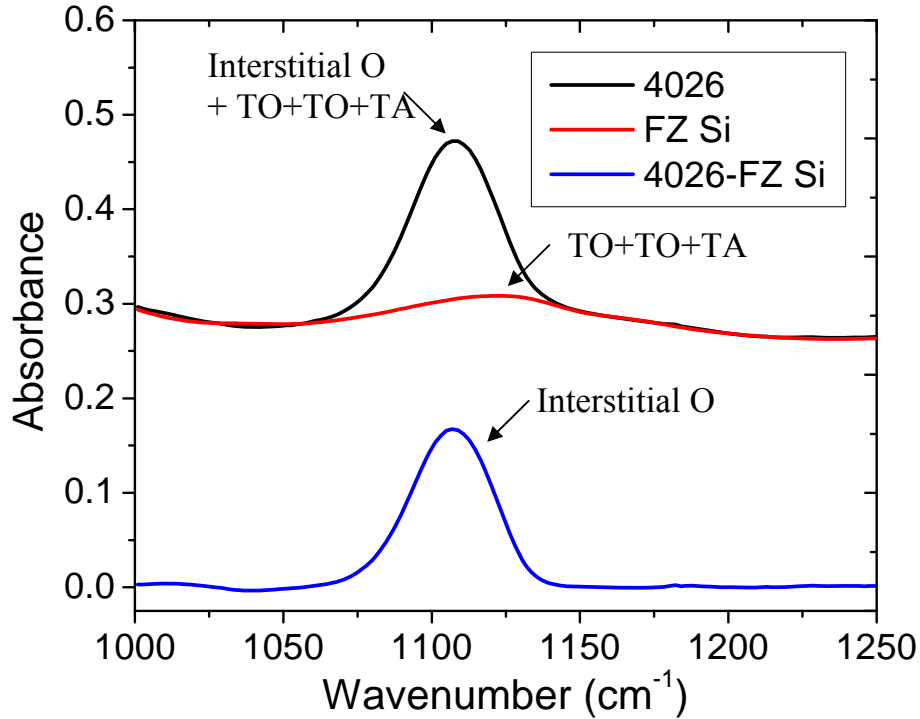
Fig. 4.6 Subtraction the three-phonon-process absorption from the spectrum of sample 4026 using FZ Si as a reference.

The origin of the interstitial oxygen here might stem from the substrate, the thermal process induced phase change during the growth or the Si/SiGe epilayers. In order to investigate the source of the interstitial oxygen, we plot the absorption spectra of the Si substrate with and without the thermal process in Fig. 4.7. The two spectra are almost identical, showing negligible effect of the thermal process on the interstitial oxygen density. We then etched the epilayers from the sample 4026, and again did the absorption measurement. By comparing with that of the as grown sample, the intensity ratio between the peak centered at 600 cm^{-1} and the one centered

at 1106 cm^{-1} remains the same after etching away all the epilayers. We thereby conclude that the interstitial oxygen is most likely from the Si substrate, which is introduced from the quartz crucible during the silicon ingot process.
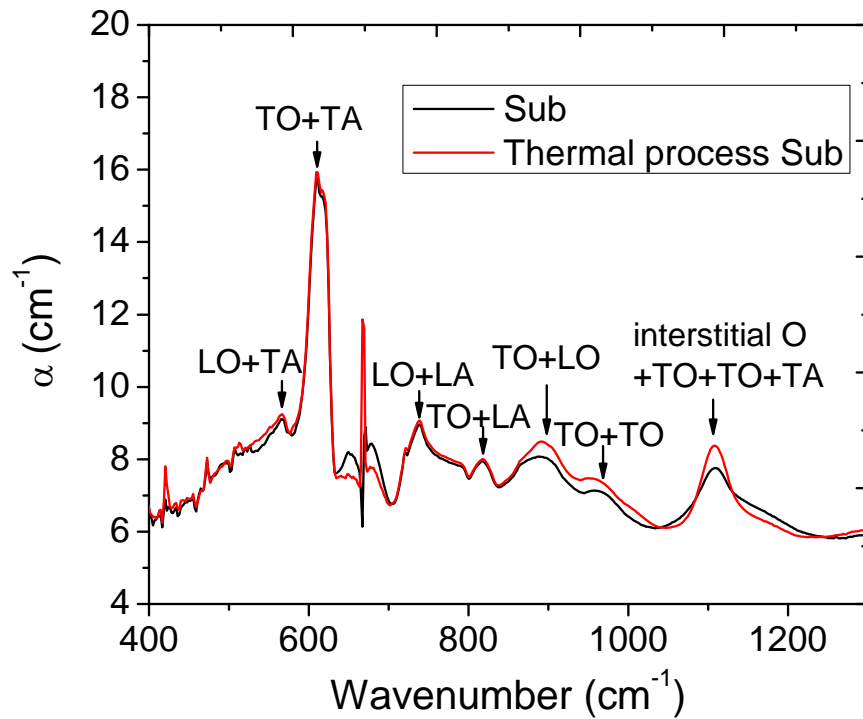
Fig. 4.7 Absorption spectrum comparison between as purchased and thermal processed Si substrate.
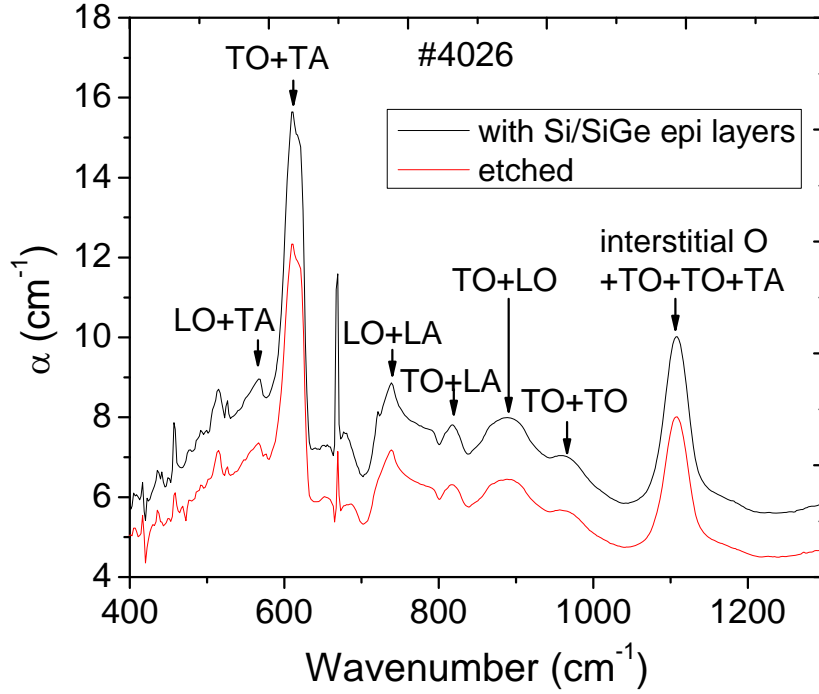
Fig. 4.8 Absorption spectrum of sample 4026 with and without Si/SiGe epitaxial layers.

To quantify the amount of the interstitial oxygen among the samples and substrates, we first do the theoretical calculation [3]:

$$\int \alpha_v dv = N_0 \frac{\pi e^2}{3\mu c} \frac{(n^2 + 2)^2}{9n} \tag{5}$$

Here α_v is the absorption coefficient at the frequency v, μ is the reduced mass of the oscillator, e is the net electronic charge, and n is the refractive index of the surrounding medium. For the best estimate, the integral is approximated by the product of α_{max}, the absorption coefficient at the band maximum and H, the full width at half maximum of the band. Thus, we get

$$N_0 = \frac{9n}{(n^2+2)^2} \frac{3\mu c}{\pi e^2} \alpha_{max} H \qquad\qquad (6)$$

As a comparison, we also use ASTM standard to measure the interstitial oxygen concentration [4-5]. At the temperature of 300K, the amount of the interstitial oxygen can be determined by $2.45 \times 10^{17} \alpha_{max}$ (atoms/cm^{-3}), with FMHM of the absorption band of 32 cm^{-1}.

The theoretical calculation and ASTM standard measurements of several samples and substrates are summarized in Table 4.2, in which the calculated and measured interstitial oxygen concentrations are in a good agreement, with the difference at the order of 10%-25%.

Sample	α_{max}(cm^{-1})	FWHM (cm^{-1})	Calculated C_{oi} ($\times 10^{18}$cm^{-3})	ASTM Coi($\times 10^{18}$cm^{-3})
3999	3.2	31	1	0.8
4026	3.6	33	1.1	0.9
Si Sub	1.1	41	0.4	0.3
TP Si sub	1.7	32	0.5	0.4

Table 4.2 Measured and calculated concentration of interstitial oxygen among different samples and substrates.

To explore the intersubband transition in the multiquantum wells, the absorption spectrum was simulated, using lorentian lineshape function and infinite quantum well to estimate the oscillator strength. To our best knowledge, most of the reported FWHM for intersubband absorption is around 15% of the peak absorption, hereby we use 15% as an estimate to do the simulation. The simulated spectrum of the intersubband absorption for MQWs, along with the measured spectrum of the

interstitial oxygen absorption for the Czachoski Si substrate is plotted in Fig. 4.9. Indeed, as we can see, the intersubband absorption peak is much broader and weaker compared with that of the interstitial oxygen absorption, with the peak value of around 100 cm^{-1} off the interstitial oxygen one. Based on this physical argument, it is reasonable to expect that the two components of the absorption peak around 1100 cm^{-1}- 1200 cm^{-1} could be resolved.
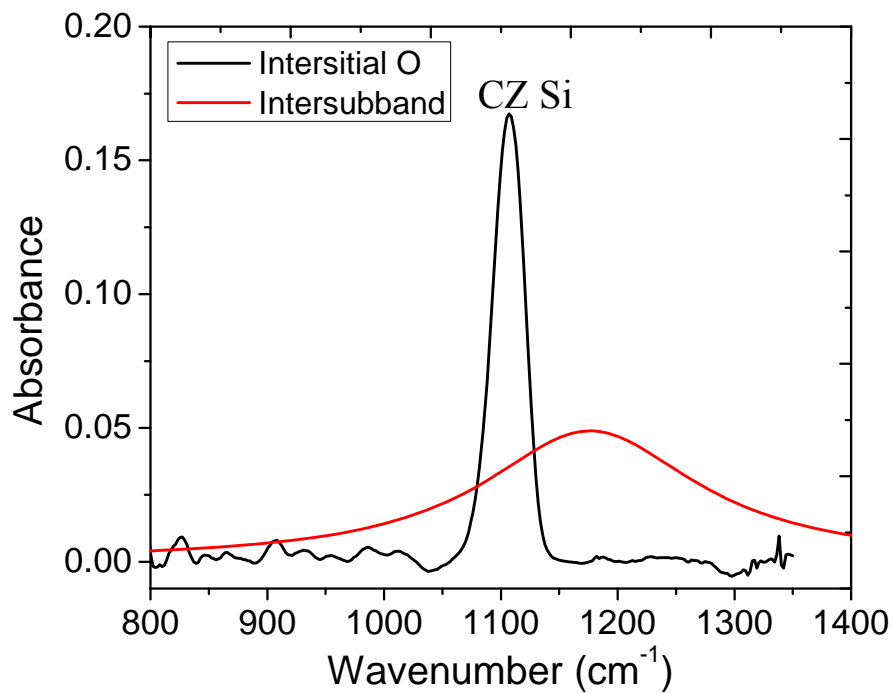

Fig. 4.9 Simulated intersubband absorption spectrum of sample 3999 with measured Czachoski Si interstitial oxygen absorption peak as a reference.

4.3 Photocurrent Measurement

4.3.1 Photocurrent Measurement in InGaAs/AlInAs/InP QCL

51

The photocurrent method is based on the photoemission of electrons or holes from the quantum wells. In contrast with the conventional intrinsic and extrinsic photoconductors, the distinct feature of the multiquantum well structure is the discreteness; that is, incident photons are only absorbed in discrete quantum wells.

Fig. 4.10 shows the experimental setup of the photocurrent measurement. Circular mesa devices of areas from 200 µm^2 to 500 µm^2 are used and reverse biased. For better coupling of the light, the IR light is shone normal to the 45° edge facet before passing through a 1000-Hz light chopper. The lock-in technique is used to obtain the voltage drop on the 470-Ω resistor and then feeds back to the FTIR.
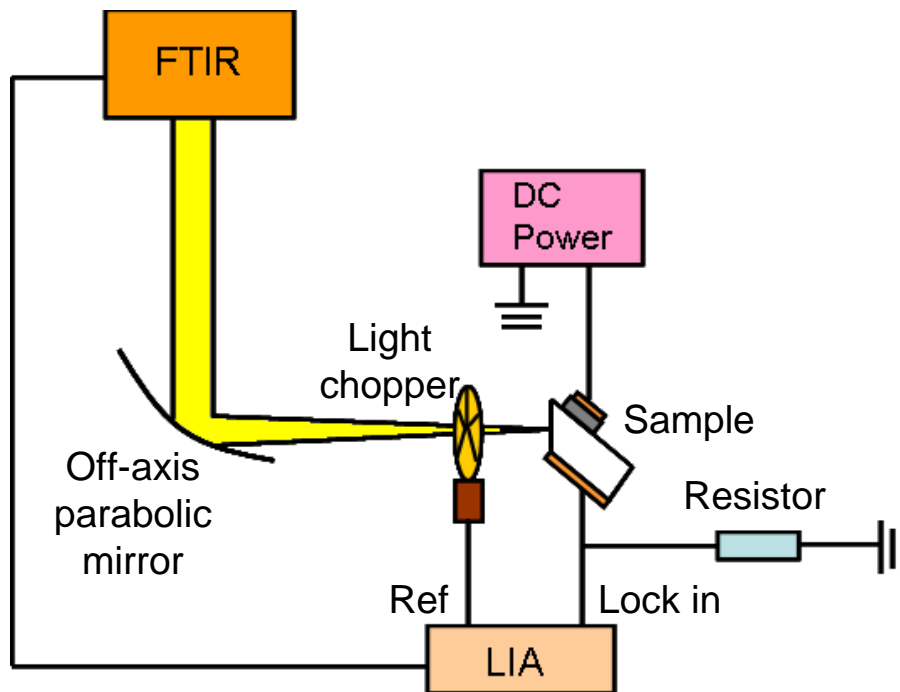
Fig. 4.10 Schematic of photocurrent measurement experimental setup.

As an example, the QC laser sample D3097 with 250 µm^2 mesa devices is at 2.5V reverse bias. The DC current on the diode is coupled by a small AC component which is induced by the photoemission, as shown in Fig. 4.11. Knowing the photoemission caused current, we can calculate the extra voltage drop on the resistor

besides the DC component. The assumption and approximation made here is that most of the voltage drop is on the diode, which is justified by the voltage-current measurements without the IR light. We finally get 540-μV AC signal on the resistor.

Fig. 4.11 Illustration of the photocurrent calculation of QC laser sample D3097. The sample was 2.5 V reverse biased. The inlets show the circuits for each experiment.

To understand the signal obtained in the lock-in amplifier, the signal process flow chart is shown in Fig. 4.12. First the locked external reference is decomposed

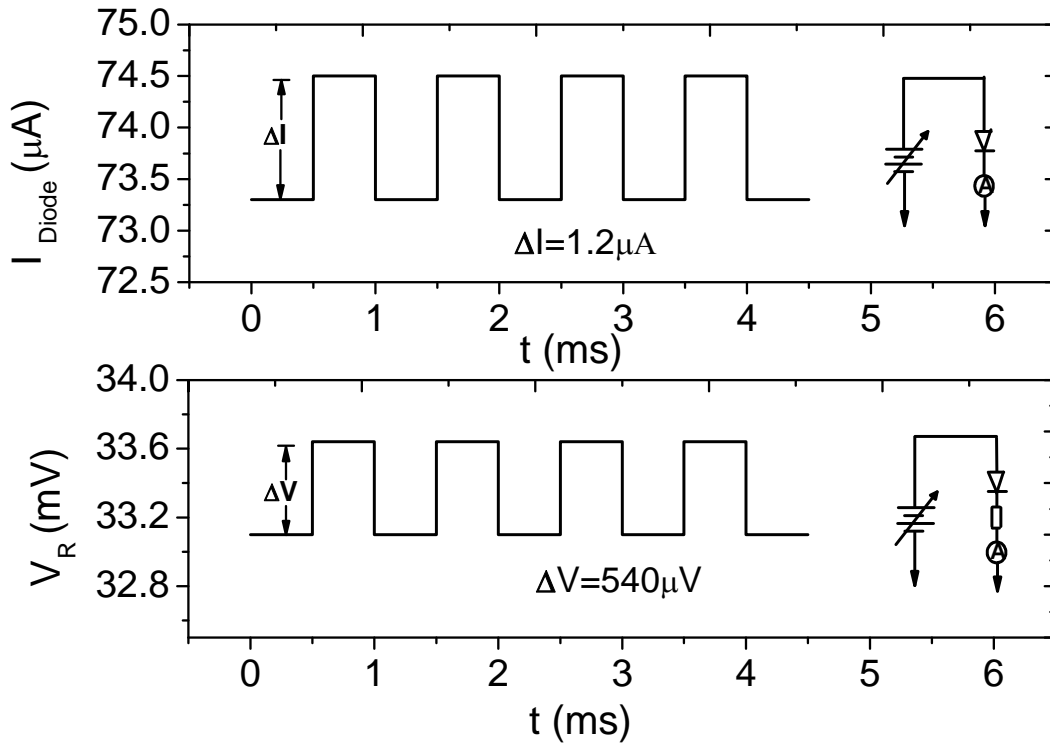into two parts, sin(ωt+φ) and cos(ωt+φ). Then, the arbitrary wave, f(t), is feed to the lock-in amplifier, where it obtains certain AC coupling and gain, and multiplied by the two components of the reference, respectively, before passing through the low path filters. Finally the two readings of A and B with 90° phase difference are displayed in the lock-in amplifier. The detailed mathematical calculation is given below.

For general wave, $f(t) = \sum a_n \sin(\varpi_n t + \theta_n)$, where $\varpi_n = n.\varpi$, the low path filter is blocked any fourier component higher than the first order. The autophase function maximizes the signal of A, with the maximum of $-1/2a_n$, while B is the minimum.

For square wave, $f(t) = \frac{4}{\pi} \sum_{n=1,3,5}^{\infty} \frac{1}{n} \sin(\frac{n\pi x}{L})$, with amplitude of 1, A is calculated as $2/\pi$. In our case, the amplitude is $\Delta V/2$, which is equivalent to $\Delta V/\pi$ for A. For the QC laser sample D3097, the reading in the lock-in amplifier is about 180 µV, which is very consistent with the calculated value, 172 µV.
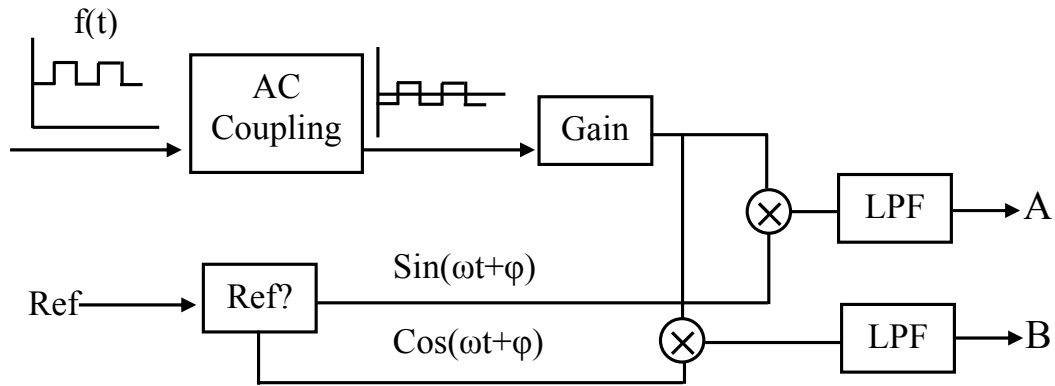
Fig. 4.12 Flow chart of the signal process by the lock-in amplifier.

Fig. 4.13 shows the photocurrent spectrum of QC laser sample D3097. The vertical axis, with arbitrary unit, is correlated with intensity of the photocurrent. The

strong peak centered at 7800 cm^{-1} might come from the epilayers, which corresponds to the intraband absorption, while the small peak at about 2200 cm^{-1} is likely from the intersubband transition of the QC structure. The two shoulder peaks on both sides of the main peak are evidently observed, while the origin of them still remains unclear.
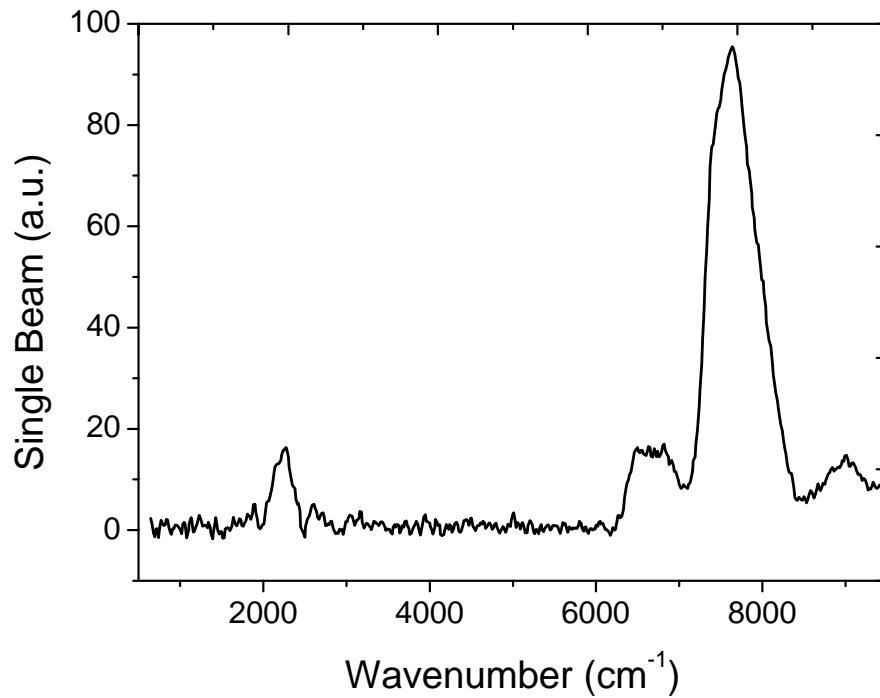
Fig. 4.13 Photocurrent spectrum of QCL sample D3097. The vertical axis is relevant to the photocurrent intensity.

4.3.2 Photocurrent Measurement in Si/SiGe MQWs

The similar photocurrent measurement is performed on the Si/SiGe Multiquauntum well structure. As shown in Fig. 4.14, a very strong peak at 10000 cm^{-1} is observed, which is due to the Si band gap absorption, while no expected signal of

intersubband transition around 1200 cm^{-1} is obtained. However, it is still uncertain that whether it is because of the experimental setup or the sample itself.
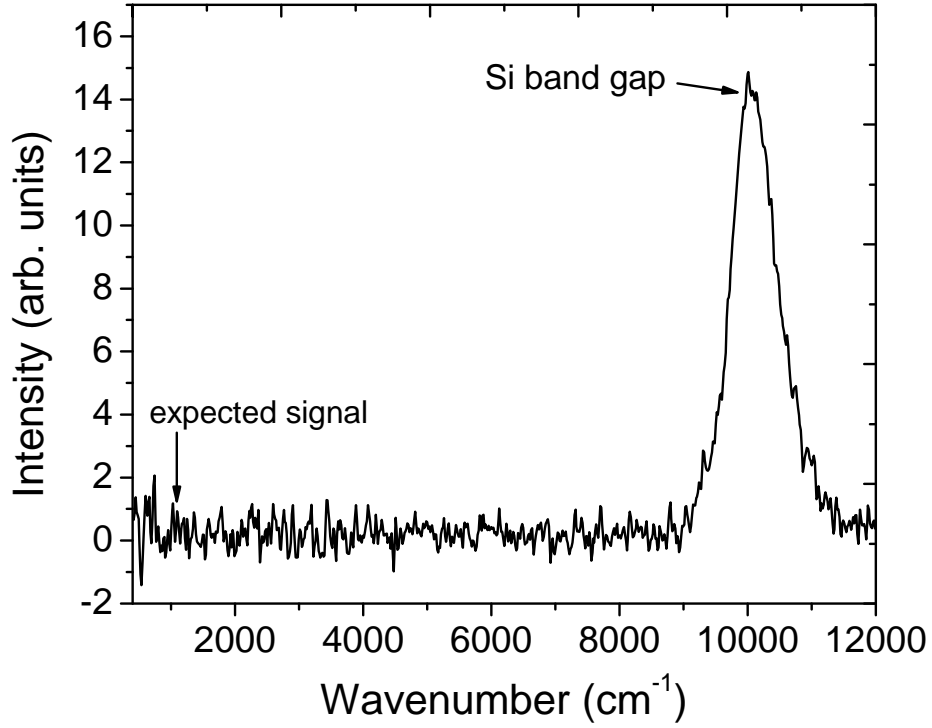
Fig. 4.14 Photocurrent spectrum of sample 3999. The only peak is related to the Si band gap.

4.4 Summary

In this chapter, we first gave a brief introduction on intersubband transition measurements in terms of multipass intersubband absorption and photocurrent measurements. We then used QC laser structures to verify both of the two experimental setups. So far we haven't obtained the intersubband transition from the

Si/SiGe multiquantum well samples. Possible obstacle underneath it has been discussed.

References

[1] C. Gmachl, F. Capasso, D. L. Sivco, and F. Y. Cho, *Rep. Prog. Phys.* **64** 1553 (2001).

[2] P. Kruck, M. Helm, T. Fromherz, G. Bauer, J. F. Nützel, and G. Abstreiter, *Appl. Phys. Lett.* **69**(22) 3372 (1996).

[3] W. Kaiser, P. H. Keck, and C. F. Lange, *Phys. Rev.* **101**(4) 1263 (1956).

[4] ASTM Designation F120.

[5] ASTM Designation F1188.

CHAPTER 5

BAND ALIGNMENT OF STRAINED SI$_{1-x}$GE$_X$ ON SI (100) HETEROJUNCTION

5.1 Introduction

Band gap engineering in Si$_{1-x}$Ge$_x$/Si structure has been investigated over the past a few decades for application of heterojunction bipolar transistors [1], modulated doped field effect transistors [2], infrared detectors [3], and etc. Recently, attempts have been made on realization of Si/ S$_{1-x}$Ge$_x$ lasers based on quantum cascade approach [4-7], which is designed by means of band-structure engineering. The Si/S$_{1-x}$Ge$_x$ heterojunction band offset, which varies with the Ge fraction, is essential for the QC laser design.

Revealing the relation of the strain, Ge fraction and the heterojunction band offsets will shed light on understanding the fundamentals of heterojunction formation, which will further assist the design and growth of the Si/S$_{1-x}$Ge$_x$ based QC structure.

In this chapter, we will study the band alignment of strained Si$_{1-x}$Ge$_x$ on Si (100) substrate. The structure was grown by RTCVD, using silane and dichlorosilane as silicon source.

5.2 Sample Growth and Structure Characterization

The Si unipolar diodes, shown in Fig. 5.1, were grown by RTCVD, using silane (10% in Ar) and dichlorosilane as silicon source, respectively. The growth pressure is 6 torr with a hydrogen carrier flow of 3 slpm. The flow rates were 10 sccm

for silane, 0.8-1.6 sccm for Germane and 26 sccm for dichlorosilane. In each sample, a p^+ Si layer with boron doping at the order of 3×10^{19} to 3×10^{19} cm^{-3} was first grown at 1000°C on a p^- substrate as a bottom contact, followed by a p^- Si layer without intentional doping grown at $625\,^{\circ}$C and $700\,^{\circ}$C for silane and dichlorosilane growth, respectively. An undoped SiGe layer with varied thickness was deposited as a precaution for heavily doped boron from diffusing to the underlying p^- Si layer. Then a 18-nm p^+ SiGe was deposited on top of the SiGe spacer, with doping ranging from 6×10^{18} to 7×10^{19} cm^{-3} and growth temperature from $525\,^{\circ}$C to $625\,^{\circ}$C. Finally a 20-50nm heavily doped (1×10^{20} to 2.8×10^{21} cm^{-3}) p+ Si layer was deposited as a top contact.
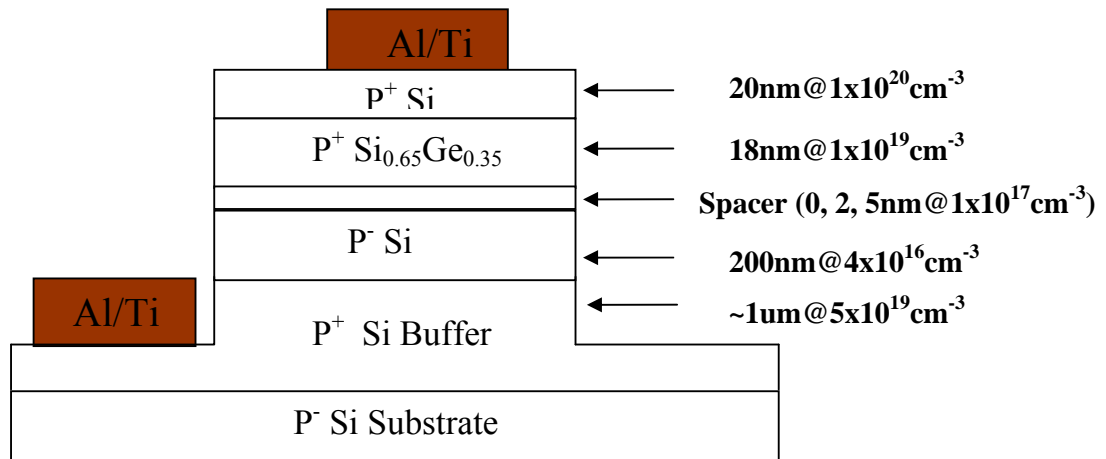

Fig. 5.1 Device structure of p^+ Si$_{1-x}$Ge$_x$/p^- Si unipolar diode.

Fig. 5.2 shows (004) X-ray diffraction (XRD) performed on the p^+ Si$_{1-x}$Ge$_x$/p^- Si diode sample 4284. The concentration of Ge, 35%, was obtained by measuring the SiGe XRD peak relative to that of the Si substrate. The value was consistent with the Ge concentration measured by high resolution SIMS.
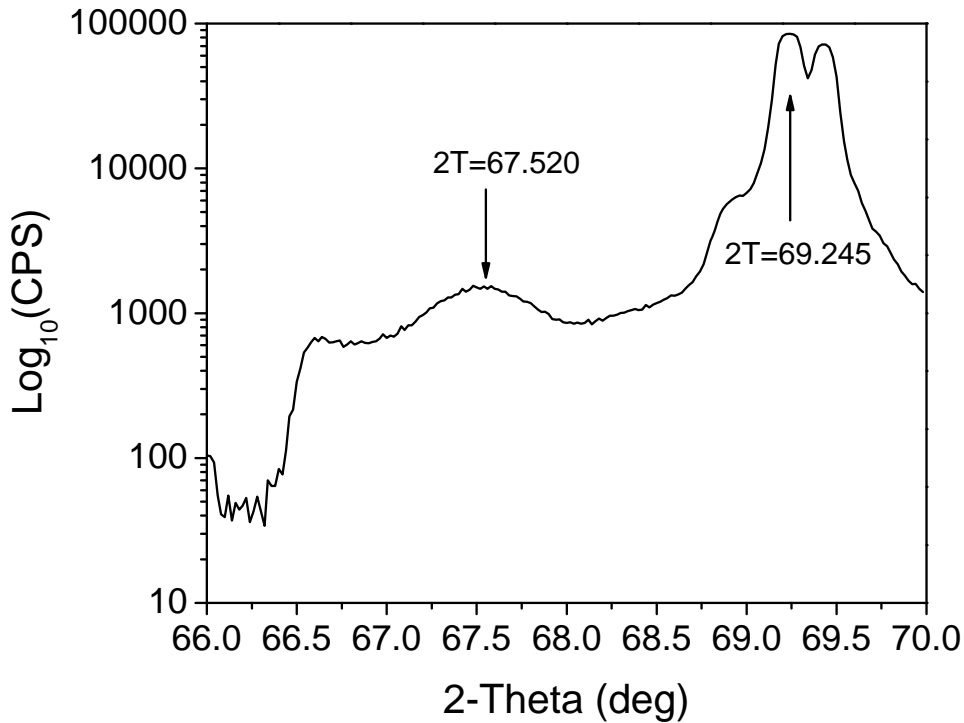
Fig. 5.2 XRD spectrum of p^+ $Si_{1-x}Ge_x$/p^- Si diode sample 4284.

5.3 Valence Band Offset of Strained $Si_{1-x}Ge_x$/Si(100) by Current-Voltage Measurement

5.3.1 $Si_{1-x}Ge_x$ Growth in SiH_4

The valence band alignment of the structure shown in Fig. 5.1 was simulated and plotted in Fig. 5.3. Under forward bias, the magnitude of hole current from the p^- Si depends on the applied voltage which shifts the valence band structure of the p^- Si relative to that of p^+ $Si_{1-x}Ge_x$. Under reverse bias ($V_{SiGe}>V_{Si}$), the valence band offset (ΔE_v) blocks the hole current from p^+ $Si_{1-x}Ge_x$, so that the device rectifies at low temperatures. Within a certain temperature range, the thermionic emission of holes

across the valence band offset determines the ideal reverse current and the hole current is exponentially dependent on temperature.
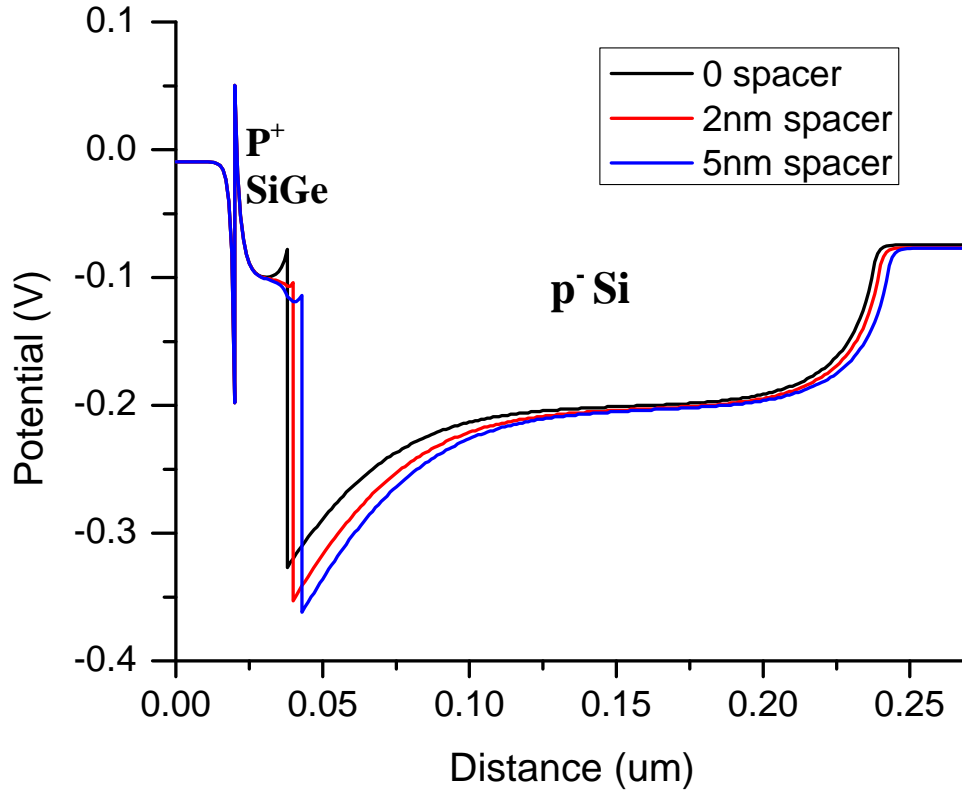

Fig. 5.3 Simulated valence band alignment of p$^+$ Si$_{1-x}$Ge$_x$/p$^-$ Si diode with varied spacers.

The expression for the thermionic current for heterojunction is slightly different from that for a metal-semiconductor contact. Here we use L.L.Change's expression [8],

$$J = A^* \frac{1}{\sqrt{T}}(1 - \frac{qV}{\Delta E_v})(e^{\frac{qV}{kT}} - 1)e^{\frac{-q\Delta E_v}{kT}}$$ (5.1)

in which, V is the applied voltage; ΔE_v is the valence band offset; and A^* is defined as the effective Richardson constant which is determined by the doping level in p⁻ Si and the valence band offset ΔE_v. It can be seen that the temperature dependence is different from that for a metal-semiconductor contact, while the thermionic current increases with the magnitude of the reverse voltage.

Two different processes were used to make Si diodes. The first one is a one-step mask process, using Al as an etching mask. The second one is a two-step mask process with SiO₂ protection layer. The mesa was made by dry etch (SF_6/CCl_2F_2=60/20), with size varied from 200μm to 500 μm, followed by Ti/Al metallization.

Fig. 5.4 shows the current-voltage characteristics for the diode sample 4284 with (a) one-step mask process, and (b) two-step mask process. The mesa size is 200μm. The diode rectifies at low temperatures and the reverse current increases dramatically with the temperature. The valence band offset of $Si_{1-x}Ge_x$/ Si can be determined by the activation energy of the thermionic current in Eq. 5.1.

The plot of $I \times T^{1/2}$ vs. 1000/T with various reverse bias voltages is shown in Fig. 5.5. In order to determine the valence band offset, the slope at very low bias voltage (-0.01V) was used due to the fact that the current does not depend on the coupling of voltage and temperature at low voltages, as seen in Eq. 5.1. Note that at -0.01V, the error caused by ($e^{\frac{qV}{kT}} - 1$) term is less than a factor of two compared to that caused by $e^{\frac{-q\Delta E_v}{kT}}$, at the temperature range we studied. Hence it is negligible.

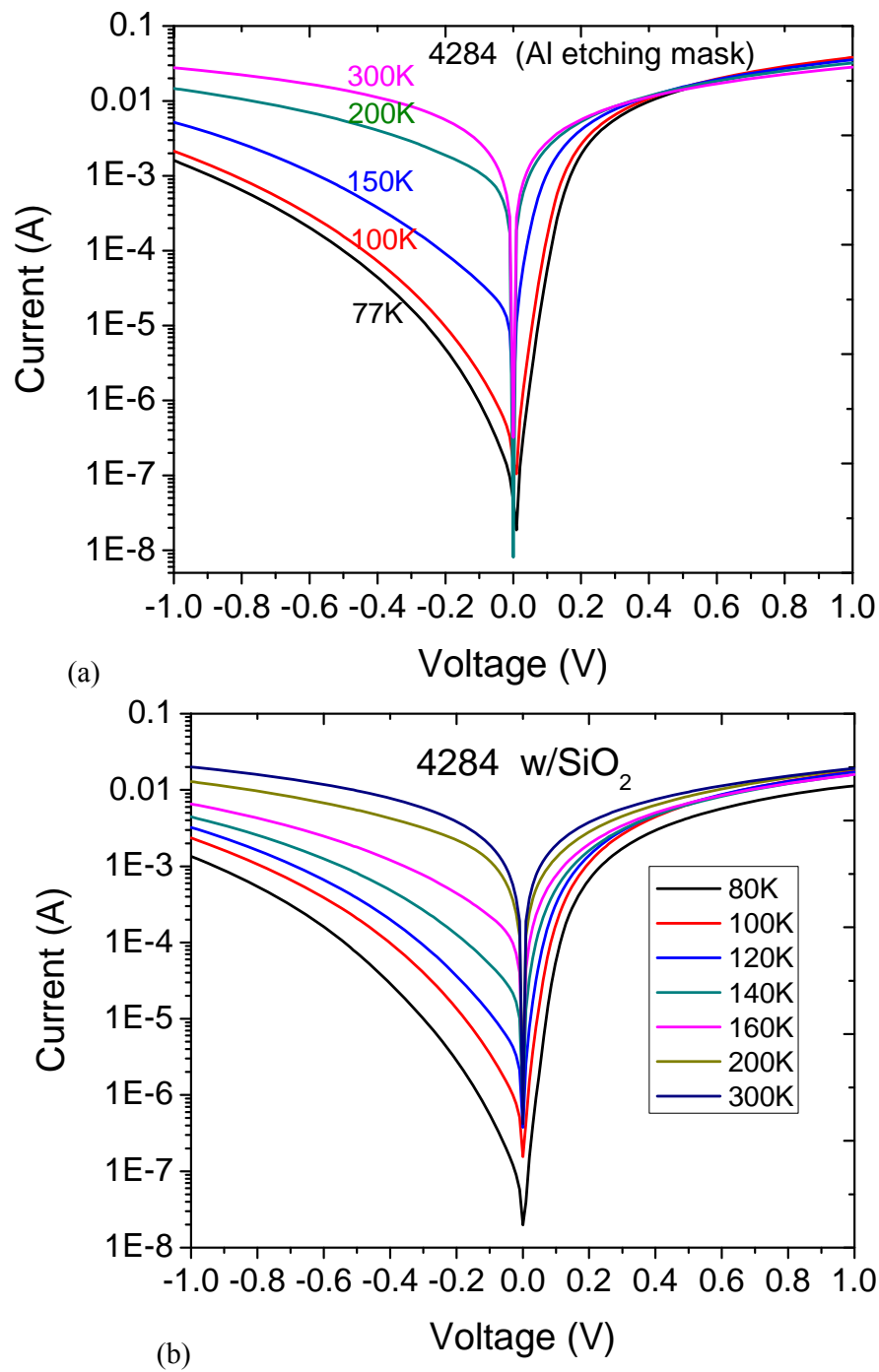Fig. 5.4 Current-voltage characteristics of the p^+ $Si_{1-x}Ge_x/p^-$ Si unipolar diode sample

4284 with silane growth as a function of temperature using two different processing

method (a) Al etching mask, and (b) with SiO_2 protection layer.

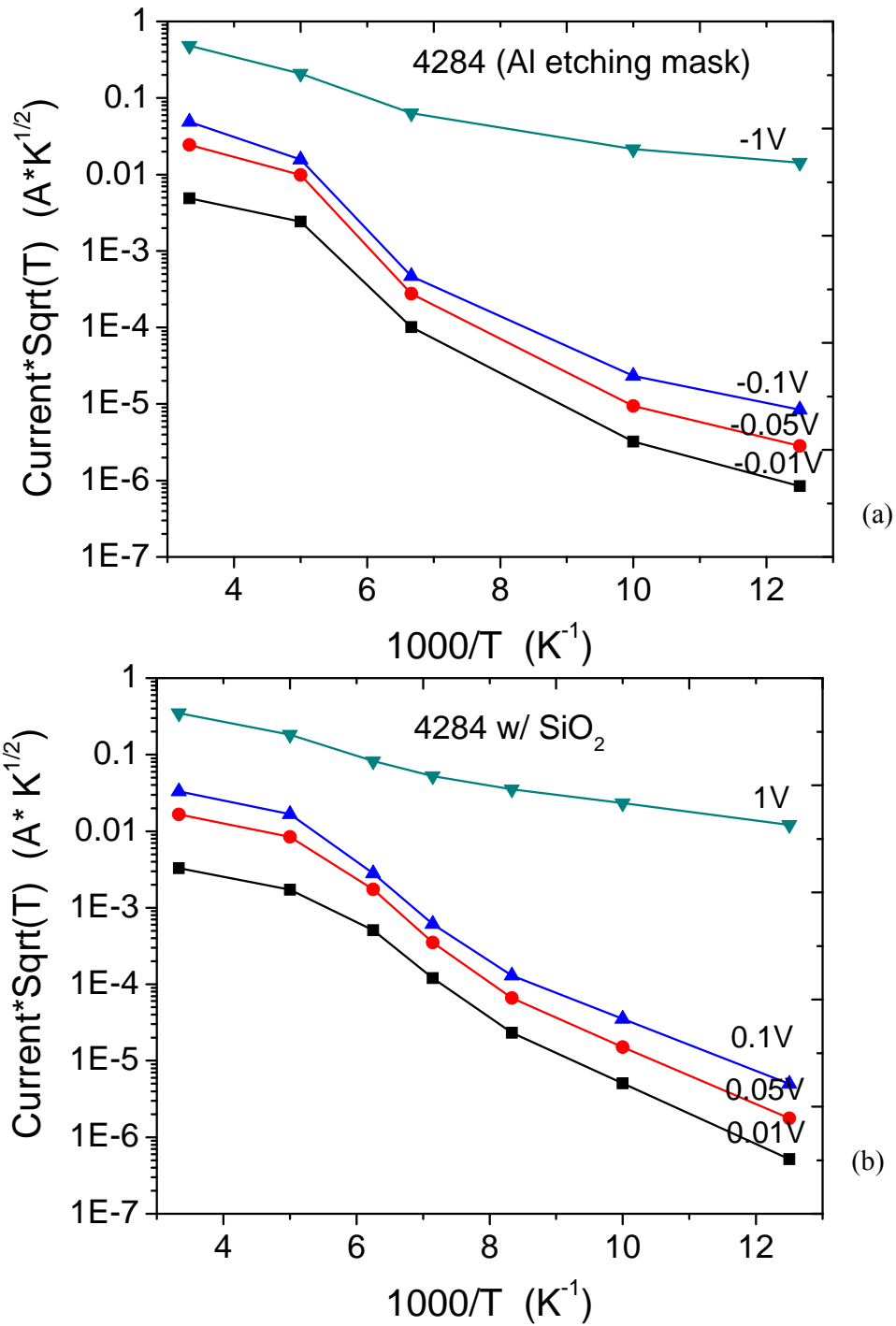Fig. 5.5 Plots of current vs temperature with various reverse-biased voltages. Plots are based on the same sample with current-voltage characteristic shown in Fig. 5.4. The valence band offset was obtained by linearly fitting the data at V=-0.01 volt.

The valence band offset for sample 4284 with 35% Ge was determined as 120 meV with the error bar of 9 meV, based on the procedure mentioned above, which is

only half of the theoretical value, 250 meV. It shows that the device process method has negligible effect on the valence band offset. We also grew several other samples with different Ge concentration, thickenss of spacers, and doping levels in p^+ $Si_{1-x}Ge_x$ and p^+ Si cap. Some of them are not rectified at low temperature; hence no band offset can be determined. The detailed results are tabulated in Table 5.1. The reason that the measured band offset deviates from the theoretical value is still unknown.

5.3.2 $Si_{1-x}Ge_x$ Growth in DCS

The same structure as that in the previous section was grown using dicholorsilane as the silicon source with 20% Ge, which is a very standard and mature growth recipe for our RTCVD growth. It was used to test the validity of the device process and the low temperature technique used in the measurements.

Fig. 5.6 shows the current-voltage characteristics for sample 4377. A much lower leakage current was observed at reverse bias, compared to that of sample 4284. The plot of $I \times T^{1/2}$ vs. 1000/T with various reverse bias voltages is shown in Fig. 5.7, from which the valence band offset was obtained as 160 meV, with an error of 5 meV. This value is very consistent with the theory (~150meV). Therefore we could conclude that the band offset deviation for sample 4284 has nothing to do with the device process or the measurement technique. However the cause of this phenomenon is still unclear.
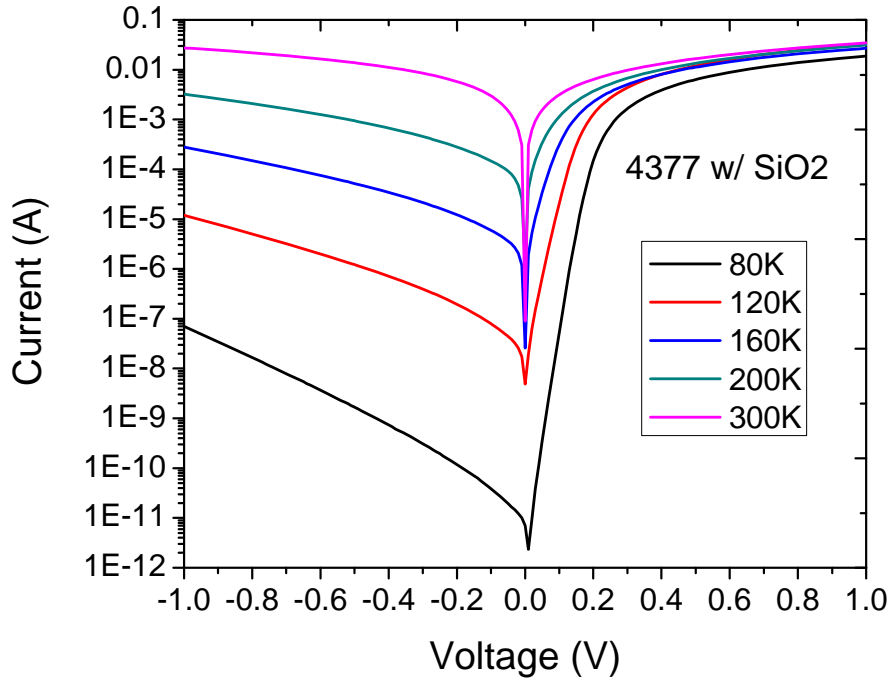
Fig. 5.6 Current-voltage characteristics of the p^+ $Si_{1-x}Ge_x$/p^- Si unipolar diode sample 4377 with dichlorosilane growth as a function of temperature.

Sample	4268	4269	4284	4421	4422	4377
Si source	SiH$_4$	SiH$_4$	SiH$_4$	SiH$_4$	SiH$_4$	DCS
Nominal Ge content (%)	35	35	35	35	20	20
Thickness of spacer (nm)	0	3	5	5	5	3
Doping level in p^+ $Si_{1-x}Ge_x$ ($\times10^{-19}cm^{-3}$)	7	7	7	0.6	0.6	1
Doping level in p^+ Si cap ($\times10^{-20}cm^{-3}$)	28	28	28	1.4	1.4	1
ΔE_v(meV)	NA	NA	120±9	60±3	NA	160±5

Table 5.1 Device structures of p^+ $Si_{1-x}Ge_x$/p^- Si diode samples.
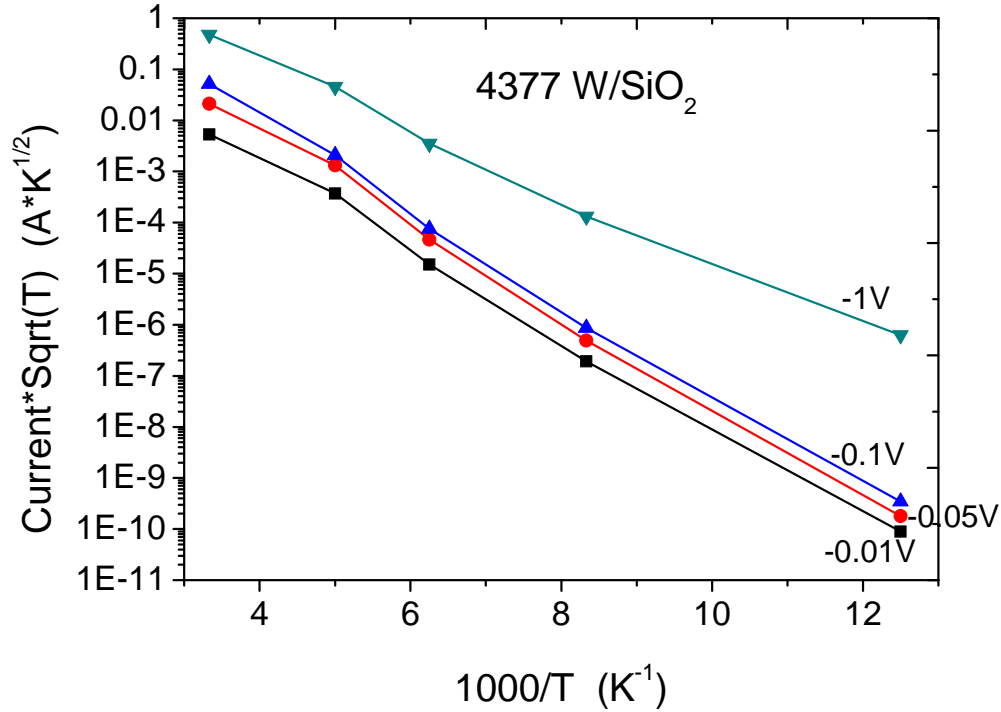
Fig. 5.7 Plots of current vs temperature with various reverse-biased voltages. Plots are based on the same sample with current-voltage characteristic shown in Fig. 5.6. The valence band offset was obtained by linearly fitting the data at V=-0.01 volt and ΔE_V=160±5 meV.

5.4 Introduction of Model ST-500-1(4CX) Low Temperature Micromanipulated Probe Station

The model ST-500-1(4CX) low temperature micromanipulated probe station, shown in Fig. 5.8, has two stage heat exchanger to ensure full use of the enthalpy of the transferred liquid nitrogen or helium. The vibration level is only +/- 25 nm. The cryostat includes two gold plated copper sample mounts. The first one with a 42-mm diameter is for working without permanent magnets, while the second one can accept a ring permanent magnet with a vertical field up to 1000 Gauss. The original design for this system only has one 50-ohm control heater and two Si diode thermometers. In

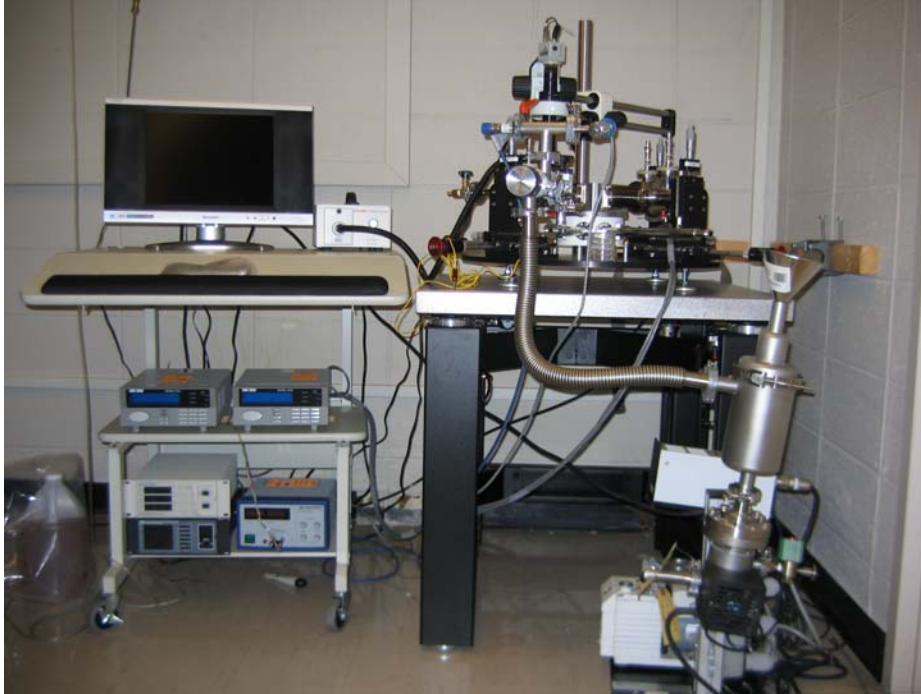order to reduce the time for heating up the chamber, we installed another heater on the radiation shield.

Fig. 5.8 Model ST-500-1(4CX) low temperature micromanipulated probe station system

.

The problems with the original probe station setup was that the sample mount was grounded and electrically connected to the radiation shield and the metal body, which means more leakage paths, and hence higher open circuit leakage current (>1 Pa). It also increased the noise level. In addition, there is no independent probe connection to the sample mount, hence inability to use the back contact.

To solve this problem, we replaced the original sample mount with an electrically isolated one and connect it to an insulated BNC connector, as shown in

Fig. 5.9. As a result, the leakage currents are down to less than 500 fA, for voltages up to 30 V. The probe station now has 5 probes, 4 top and 1 bottom.
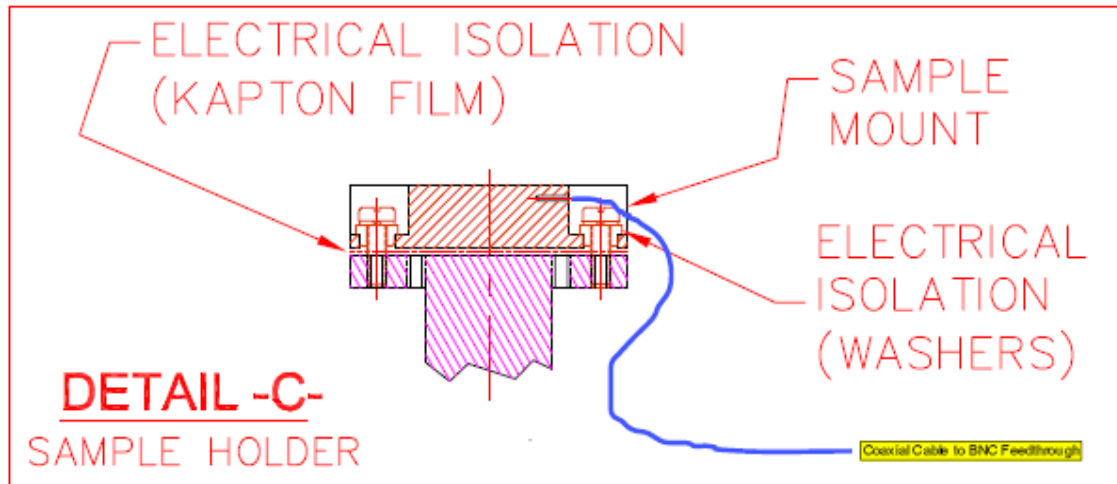

Fig. 5.9 Schematic of the electrical isolation of the sample mount.

5.5 Summary

In this chapter, we discussed the electrical characterization method to determine the valence band offset of compressively strained $Si_{1-x}Ge_x$/Si. As a result, the silane-based samples have much smaller band offset, compared to the theoretical value, while the DCS-based sample gives reasonable value. It seems that changing the doping levels in p^+ $Si_{1-x}Ge_x$/Si layer and the thickness of $Si_{1-x}Ge_x$/Si spacer has no obvious effect on this deviation of valence band offset. The cause of this phenomenon is still unclear.

References

[1] S. S. Iyer, G. L. Patton, J. M. C. Stork, B. S. Meyerson, and D. L. Harame, *IEEE Trans. Electron Devices* **ED-36** 2043 (1989).

[2] H. Daembkes, H. J. Herzog, H. Jorke, H. Kibbel, and E. Kasper, *IEEE Trans. Electron Devices* **ED-33** 633 (1986).

[3] T. L. Lin, A. Ksendzov, S. M. Dejewski, E. W. Jones, R. W. Fathauer, T. N. Krabach, and J. Maserjian, *IEEE Trans. Electron Devices* **ED-38** 1141 (1991).

[4] G. Dehlinger, L. Diehl, U. Gennser, H. Sigg, J. Faist, L. Ensslin, D. Grützmacher, and E. Müller, *Science* **290** 2277 (2000).

[5] L.Diehl, H. Sigg, G. Dehlinger, D. Grützmacher, E. Müller, U. Gennser, I. Sagnes, T. Fromherz, Y. Campidelli, O. Kermarrec, D. Bensahel, and J. Faist, *Appl. Phys. Lett.* **80(18)** 3274 (2002).

[6] L. Diehl, S. Mentese, E. Müller, D. Grützmacher, H. Sigg, U. Gennser, I. Sagnes, Y. Campidelli, O. Kermarrec, D. Bensahel, and J. Faist, *Apply. Phys. Lett.* **81** 4700 (2002).

[7] G. Scalari, S. Blaser, J. Faist, H. Beere, E. Linfield, D. Ritchie, and G. Davies, *Phys. Rev. Lett.* **93** 237403 (2004).

[8] L. L. Chang, *Solid State Elec.* **8** 721 (1965).

CHAPTER 6

SUMMARY

We have reported p-type Si/SiGe multiple quantum wells for intersubband transitions, grown by rapid thermal chemical vapor deposition with excellent well to well uniformity, as measured through high resolution secondary ion mass spectroscopy and cross sectional transmission electron microscopy. Critical factors are the use of a silane source for low background doping, the growth of the SiGe layer at a lower temperature to achieve a low growth rate, and repeatable temperature control.

Two methods, multipass transmission and photocurrent measurements, are used to study the intersubband transitions in the multiquantum wells. So far, no intersubband absorption has been obtained throughout all the Si/SiGe samples. The underlying obstacles are still in investigation.

The electrical characterization method has been used to verify the valence band offset of the Si/SiGe multiquantum wells. It shows a big deviation, only half of the theoretical value, for growth based on silane.